RSC Advances




ROYAL SOCIETY OF CHEMISTRY

www.rsc.org/advances

# Porous ternary Fe-based catalysts for oxidative dehydrogenation of ethylbenzene in the presence (absence) of carbon dioxide

Nuryana A. Ferreira[a], Josué M. Filho[b], Alcineia C. Oliveira[c*]

[a]Universidade Federal do Ceará, Campus do Pici-Bloco 940, Fortaleza, Ceará, Brazil. Phone/fax: 55 85 33 66 90 51/ 9982 *Corresponding author: alcineia@ufc.br

[b]Universidade Federal do Ceará, Departamento de Física,Fortaleza, Ceará. Phone/fax: 55 85 3366 94 83.

*Author for correspondence

**Abstract**

Porous ternary Fe-based catalysts were characterized and their catalytic properties through the oxidative dehydrogenation of ethylbenzene in the presence of carbon dioxide (ODH) or its absence (DH) were investigated. The catalysts were characterized by X-ray diffraction (XRD), chemical analyses, termoprogrammed reduction (TPR), physisorption measurements, Raman spectroscopy and scanning electron microscopy coupled to energy dispersive X-ray spectrometry (SEM-EDX). Kinetic modeling of reverse water gas shift reaction (RWGS) and the effects of reaction parameters, such as reaction temperature and $CO_2/H_2$ ratio on the catalytic activity were also investigated. Addition of Zn, La, Mg or Ni promoters to porous Fe-based solid greatly enhanced ODH reaction whereas RWGS one is favoured by Ni promotion. The $CO_2/H_2$=1 ratio and temperature of 850K were the best condition for RWGS occurrence. The implications of these conditions on the application of catalysts for ODH and DH reactions were discussed. Ethylbenzene conversions were too low due to the decreased textural properties of some catalysts and selectivity to styrene is inhibited as well. Porous FeAlZn catalyst exhibited higher catalytic performance than the other ternary solids in terms of the ethylbenzene dehydrogenation and resistance against deactivation whereas low RGWS conversions were observed under the abovementioned conditions.

Keywords: dehydrogenation, ethylbenzene, RWGS, Fe-based oxides, characterizations.

## 1. Introduction

Chemical recycling of carbon dioxide from combustion sources is a sustainable energy process, since it allows the strategy to capture and storage $CO_2$ for reducing its emissions. In this sense, the use of $CO_2$ as a mild oxidant in catalytic reactions has been strongly encouraged. Moreover, alternatives technologies for using carbon dioxide such as wet partial oxidation or autothermal reforming, propane dehydrogenation, ethylbenzene dehydrogenation, dry reforming, among others[1-3], represent further remarkable economic advantages of $CO_2$ consumption.

Additionally, the growing concern about costs for styrene production has directed the interest of researchers toward the development of oxidative dehydrogenation of ethylbenzene in the presence of carbon dioxide (ODH). Styrene is a high valuable monomer used for polymeric polystyrene resins and styrene–butadiene rubbers production[1-11]. However, the commercial process of direct steam dehydrogenation of ethylbenzene (DH) to styrene leads to the use of large amount of superheated steam.

Another limitation of the process is the low selectivity to styrene due to benzene and toluene by-products formation besides the thermodynamic equilibrium limitations[6-10]. Thus, ODH reaction in the presence of carbon dioxide offers advantages over DH reaction owing to $CO_2$ reducing the energy consumption, accelerating the reaction rate, prolonging catalyst lifetime, enhancing selectivity, alleviating the thermodynamics constraints and it could indeed drives the process towards green chemistry[1-10].

The findings state that the DH reaction is coupled with reverse water gas shift (RWGS). Because RWGS reaction is mildly endothermic with enthalpy of 41.1 $kJ.mol^{-1}$, the reaction is carried out at low temperatures. This makes the coupled process of ODH reaction slight endothermic compared to DH [9]. Albeit the isolated RWGS reaction has no such difficulties, catalytic stability is often poor and the solid is still not developed enough for industrial application, although it has been widely investigated on a laboratory scale. Additionally, RWGS reaction occurrence is undesirable for ethylbenzene dehydrogenation, dry reforming, propane oxidation among others reactions due to the low yield of the products from these reactions achieved[5,12-14]. Indeed, the kinetics of the RWGS reaction is studied at low conversion and high hydrogen partial pressure and the reaction should be limited by dissociative $CO_2$ adsorption.

Systematic exploitation of dehydrogenation of ethylbenzene coupled to RGWS would accomplish a major efficiency of styrene production and reduction in carbon dioxide emissions. A great deal of insight into the coupling reaction has been acquired by studying the catalytic activities of various solids based on iron oxides. Nanostructured Fe-containing promoters such as alumina, zirconia or ceria have shown good performance for catalyzing the oxidative dehydrogenation of ethylbenzene (EB) with $CO_2$. Noteworthy, the activity of *in situ* $FeAl_2O_4$ spinel phase formation motivated us to investigate the catalytic properties of FeAl solid by adding a third element in catalyst composition[10]. As the stability of $FeAl_2O_4$ phase in ODH reaction is limited owing to carbonaceous deposition, there is need to develop new catalyst systems that allow for uniform dispersion of the active phase as well as high stability and drive the redox mechanism of the titled reaction to avoid RGWS reaction isolated occurrence. The addition of La, Mg, Zn or Ni in the Fe-based solids is expected to minimize the deactivation by phase transformation effects.

Thus, the aim of this work is to investigate the performance of nanostructured FeAlZn, FeAlLa and FeAlNi catalysts for styrene production. FeMgZn is used for comparisons purposes. Also, a deep comprehension of the DH and RWGS reactions conditions to improve the reaction yields or avoiding their occurrence is highly desirable, depending on the investigation focus. This work presents kinetic modeling and catalytic results to evaluate the effect of the temperature and $CO_2/H_2$ ratio on the catalytic properties of Fe-based catalysts through the RWGS and DH reactions. The investigations of the adsorption and deactivation constants as well as the rate of the RWGS reaction in different temperatures are also studied by the model.

## 2. Experimental

### 2.1. *Catalysts preparation*

The mixed oxides were prepared by precipitation method using aluminum tri-sec-butoxide ($Al(OC_4H_9sec)_3$) and ferric nitrate $Fe(NO_3)_3 9H_2O$, as precursors[10]. In brief, aluminum tri-sec-butoxide was first dissolved into excess of isopropanol and vigorously stirred at 333K till the solution became homogeneous. Then, a mixture of 2.9 mol of water, ferric nitrate, 6.5 mol of absolute ethanol together with lanthanum nitrate solution was added to the stirred mixture of aluminium through a peristaltic pump. The reactants were maintained under constant stirring

and refluxing for 24 h. The gel was afterwards, washed with ethanol, dried at room temperature and calcined at 873K under air flow at a heating rate of $5^{o}C.min^{-1}$ during 2 h. The abovementioned methodology was used to obtain the FeAlLa. Other solids such as FeAlZn, FeAlNi and FeMgZn, in which the, zinc, nickel and magnesium nitrate, were the active component precursors. The metal contents measured by chemical analyses were 20:20:60 mol%, respectively for iron and aluminium and the third metal added to the solid.

*2.2. Characterization*

X-ray diffraction patterns (XRD) were measured on a PANalytical X'PERT HighScore's X-Ray diffraction equipment, under the following conditions: Cu target Kα ray, scanning step of $0.02^{o}$, scanning current, scanning rate of 0.1 and voltage of 20 mA and 30 kV, respectively. The diffractograms were compared to those of JCPDS (Joint Committee on Powder Diffraction Standards).

Inductively Coupled Plasma Optic Emission Spectroscopy (ICP-OES) was performed with a Varian apparatus. Previously, the solids were digested with an equimolar mixture of nitric and hydrochloric acids at $90^{o}C$ in a sand bath. The actual metallic content of the solids were then determined by ICP-OES.

The adsorption/desorption isotherm experiments were carried out with a ASAP 2000 Micromeritics instrument to determine the specific surface areas and pore structure parameters of the solids. The probe molecule was nitrogen at 77K surface area analyzer. Samples were degassed at 423K for 12 h, prior to measurement. The BET equation was used to calculate the total specific surface areas of fresh and spent catalysts. The pore distributions and surface areas of mesopores were calculated by Barret-Joyner-Halenda (BJH) method to the desorption branch of the isotherms.

The morphological aspects of the sample were determined by Scanning Electron Microscopy (SEM) measurements using a using a FEG Quanta 450 electron microscope equipped with an EDS Bruker QUANTAX system coupled to the SEM microscope, using an acceleration voltage of 2 kV.

Temperature programmed reduction ($H_2$-TPR) experiments were performed in a home-made equipment using a quartz tube reactor possessing a inner diameter of 6 mm and coupled to a thermal conductivity detector-TCD for monitoring the hydrogen consumption. The mass

of catalyst was 50 mg and the experiment was lead in the range of 323-1273K. A mixture of 8% $H_2/N_2$ was used as reducing gas with a rate of 100 mL.min$^{-1}$, after passing through a 13X molecular sieve trap to remove water. Before the analysis, samples of ca. 0.1 g were placed in tube reactor and heated under nitrogen at 373K for 2 h.

Spent catalysts were characterized by Raman spectroscopy. The Raman measurements were obtained on a LabRam spectrometer (JobinYvon) under ambient conditions. A 532 nm argon ion laser was used as the exciting source on the sample surface and a power of 2 mW. Ten accumulated spectra were obtained in each spectral range and the spectral resolution was 3 cm$^{-1}$ in the 5–2000 cm$^{-1}$ range. The Olympus lens focus was of 100 times.

*2.3 Catalytic testing*

The dehydrogenation of ethylbenzene by $CO_2$ was carried out under steady-state conditions in a quartz fixed bed reactor. The reactant mixture was composed of carbon dioxide and ethylbenzene at a 30:1 ratio, respectively. The flow rates used were as follows: $N_2$, 11.7 mmol·h$^{-1}$; $CO_2$, 58 mmol·h$^{-1}$; and EB, 1.98 mmol·h$^{-1}$ ($CO_2$/EB molar ratio of 30). The catalyst (50 mg) was crushed and activated *in situ* under a flow of nitrogen and was heated from room temperature to 823K over the course of 1 h to remove any gaseous impurities from the surface of the catalyst. The reaction was performed under atmospheric pressure at a temperature of 823K, previously defined by theoretical and experimental studies[5].The product was analyzed by gas chromatography (GC) using a Simple Chrom chromatograph equipped with flame ionization detector-FID and thermal conductivity detector-TCD. GC analyses were carried out at isothermal conditions from 295 to 523K with a rate of 283K. min$^{-1}$ and injector temperature of 523K.

The conversion and selectivity were defined as follows

$$\%\ \text{EB Conversion} = \frac{EB_{in} - EB_{out}}{EB_{in}} \times 100 \qquad \text{(I)}$$

$$\%\text{EB selectivity} = \frac{\text{mol of desired product}}{\text{mol of reacted ethylbenzene}} \times 100 \qquad \text{(II)}$$

Prior to the catalytic tests, modeling of DH[5] and RWGS reactions without catalyst was performed to identify the best reaction conditions to perform the experimental analyses.

*2.1. Model*

Modeling of the experimental data is well suited to quantify the kinetic and thermodynamic effects of the RWGS reaction without using the catalysts. To include possible temperature, $H_2$/CO ratio and pressure effects on the Fe- catalyzed RWGS reaction, it is necessary to model the data. Thus, the thermodynamic–kinetic assessment was implemented and solved in the $C^{++}$program in the 400-1100K temperature range. The reaction rates have been taken into consideration to define the optimal conditions to operate the reaction.

*2.1. 1. Kinetic modeling*

Kinetic model considers that the reverse water gas shift reaction (RWGS) is formally regarded as a single-step surface reaction (reaction (I)). The $CO_2$ is assumed to be directly transformed into carbon monoxide and an oxygen radical by dissociative adsorption (reaction II):

$$CO_2\,(g) + H_2\,(g) \rightleftharpoons CO(g) + H_2O(g) \quad \Delta H°_{298.15K} = 41.17 \text{ kJ mol}^{-1} \qquad (I)$$

$$CO_2(g) \rightleftharpoons CO\,(g) + O\bullet \qquad (II)$$

Hence, the rate of carbon dioxide consumed, $-r'CO_2$, is proportional to carbon monoxide produced , $r'CO$, being the reaction II the determinining step of the reaction:

$$-r'_{co2} = r'_{co} = k_{co2}\left(P_{co2}C_v - \frac{P_{co}.C_{o.s}}{K_{co}}\right) \quad (1)$$

where $k_{CO2}$; is the kinetic constant of velocity for $CO_2$ and $P_{CO}$ is the partial pressure of CO. The ratio between the adsorption and desorption constants of CO is given as $K_{CO}$. Also, it is assumed that the total amount of active sites occupied by oxygen atom and the number of active surface sites available per catalyst mass are equal to *CO.S* e and *Cv*, respectively.

The first approach used for RGWS reaction assumes the fact that the adsorbed oxygen reacts with hydrogen from the gas phase, derived from Eley-Rideal mechanism expression, as given below in reaction III[15].

$$H_2(g) + O\bullet \rightleftharpoons H_2O(g) + \bullet \qquad (III)$$

Thus, the rate of water produced consumed, $r'H_2O$, expressed in the Eq. (2).

$$r'_{H2O} = k_{H2O}\left(P_{H2}C_V - \frac{P_{H2O}.C_V}{K_{H2O}}\right) \quad (2)$$

In a second approach the kinetics for the system under study adopts the steady state condition for RWGS reaction in which the rate of distinct and discreet sites generation is zero and the following expression is presented for rate of carbon dioxide:

$$-r'_{CO2} = \frac{k_{CO2}C_T\left(P_{CO2} - \frac{P_{CO}.P_{H2O}}{P_{H2}K_{CO2}K_{H2O}}\right)}{1 + \frac{P_{H2O}}{P_{H2}K_{H2O}}} \quad (3)$$

The Eq (3) can be simplified by considering that $kCO_2$ is the ratio between adsorption and desorption constants, since the former constant is much higher than the second constant, the expression is summarized as :

$$-r'_{CO2} = k_{CO2}P_{CO}C_T \quad (4)$$

*2.1. 2. Adsorption constants*

Most simulation studies employ previously published adsorption constants expressions for similar catalysts in RWGS reaction. The dependence of the temperature on adsorption of water and $CO_2$ constants can be calculated based on the following equations:

$$K_{H2O} = K^*_{H2O}\, exp\left[\frac{\Delta H_{H2O}}{R}\left(\frac{1}{T} - \frac{1}{298{,}15}\right)\right] \quad (5)$$

$$K_{CO2} = K^*_{CO2}\, exp\left[\frac{\Delta H_{CO2}}{R}\left(\frac{1}{T} - \frac{1}{298{,}15}\right)\right] \quad (6)$$

Where $K_{H2O}$ and $K_{CO2}$ are the adsorption of water and $CO_2$ constants, respectively; $K^*_{H2O}$ and $K^*_{CO2}$ values are respectively $3.52x10^{41}$ $bar^{-1}$ and $1.24x10^{69}$ $bar^{-1}$. The enthalpy values for

water and $CO_2$ at 298.5 K ($\Delta H_{H2O}$ e $\Delta H_{CO2}$) are respectively 393.5 kJ.mol$^{-1}$ and 393.8 kJ.mol$^{-1}$ [16].

The term used to quantify the attenuation of the velocity rate by of $CO_2$ and water adsorption on the catalyst surface, $\theta$, is given in Eq(7)

$$\vartheta = \frac{1}{1 + K_{H2O} f_{H2O} + K_{CO2} f_{CO2}} \quad (7)$$

Accordingly, the term used to quantify the attenuation of the velocity rate by of $CO_2$ and water desorption on the catalyst surface, $\theta_d$, is described as follows Eq (8):

$$\vartheta_d = \frac{1}{1 + (K_{H2O})_d f_{H2O} + (K_{CO2})_d f_{CO2}} \quad (8)$$

Where $f_{H2O}$ and $f_{CO2}$ represent the fugacity of water and $CO_2$ . The values of $K^*_{H2Od}$ and $K^*_{CO2d}$ are 2.02 x10$^{-3}$ bar$^{-1}$ e 9.89 x10$^{-3}$ bar$^{-1}$ , respectively. The enthalpy values for water and $CO_2$ at 298.5 K ($\Delta H_{H2Od}$ e $\Delta H_{CO2d}$ ) are 41.3 kJ.mol$^{-1}$ e 204.0 kJ.mol$^{-1}$, respectively[16-18]. These values were also used to determine the terms that quantify the both water and $CO_2$ adsorption capacities during the deactivation of the catalyst, that is to say $K_{H2Od}$ e $K_{CO2d}$.

By summing up the reaction rates, the values of the kinetics constants for adsorption, $\theta$, *and* desorption, $\theta_d$, are determined in Eqs (9,10).

$$k'_a = k_a \theta_a \quad (9)$$

$$k'_d = k_d \theta_d \quad (10)$$

It is important to note that $k_a$ and $k_d$ are previously determined by Eq.4 at 850K, being respectively 0.32 s$^{-1}$ and 0.33s$^{-1}$.

The velocity rate of *RGWS* is also predicted by varying the partial pressure of carbon dioxide and hydrogen to obtain the optimal conditions for $CO_2/H_2$ trough reaction I[18], as shown in Eq (11).

$$r_{RGWS} = 3{,}22.10^{-6} . e^{\frac{-73600}{RT}} . \frac{P}{T^3} . p_{H2} . p_{CO2} \quad (11)$$

*2.1.3. Experimental results in RWGS*

Experimental results in RWGS were carried out by using the most actives solids. The Fe-Co based catalyst possessing a metal-to-iron ratio of 3 was synthesised according to a method previously described[15] and calcined at 873K under air flow. This catalyst was chosen due to their excellent structural and textural properties, which promoted the dry reforming of methane[19] and showed to be potential catalysts for RWGS.

The reverse water gas shift reaction was carried out in a microcatalytic system was in a quartz tubular fixed bed reactor. About 150 mg of catalysts were used with the reactor operating at different temperatures and a mixture of 5%$CO_2/N_2$ in a hydrogen atmosphere was introduced into the catalyst bed using a flow of 40 mL $min^{-1}$. The $H_2/CO_2$ molar ratio was 1:1 and the products of the reaction were analysed in a Varian chromatograph. Previously, the catalysts were in situ activated at 873K under 5%$H_2/N_2$ for 1 h.

## 3. Results and discussion

*3.1. Characterizations of the catalysts*

*3.1.1. XRD, textural properties and SEM-EDX*

Fig. 1 shows the XRD patterns of the catalysts. All of the XRD possess relatively high intense lines describing the crystalline character of the solids, except for FeAlLa. The latter exhibits diffuse diffraction peaks at 2θ = ca. 35°, which is attributed to the typical amorphous character of $La_2O_3$-$Al_2O_3$[20]. Additionally, the characteristic difractogram of FeAlLa could be attributed to $La_2O_3$ (JCPDS, 05-0602), $LaAlO_3$ (JCPDS 85- 1071) or $LaAl_{12}O_{19}$ and (JCPDS, 77-0335) phases or yet γ- $Al_2O_3$ (JCPDS, 10-04625). However, due to the broadness of the peaks, their presence is not determined. Besides, the reflections belong to iron phases are not observed probably due to their nanometric sizes or good dispersion in $La_2O_3$-$Al_2O_3$ matrix. This feature is commonly found in materials prepared by sol-gel method [21,22].

Fig.1

It is obvious that FeAlZn has diffraction peaks assigned to γ-$Fe_2O_3$ (JCPDS 39-1346), ZnO (JCPDS, 89-0510) and γ-$Al_2O_3$ (JCPDS, 10-04625). Mixed oxides phases such as $ZnAl_2O_4$ or $ZnFe_2O_4$, $Fe_2O_3$–$Al_2O_3$ could be formed, but calcinations temperatures are too low to obtain these mixed oxides. XRD pattern of FeMgZn displays MgO (JCPDS 18-1022), besides those

of ZnO and γ-$Fe_2O_3$. The diffraction lines do not show any diffraction peak relative to $MgFe_2O_4$ due to the low heating temperature of the solid to generate this phase [23]. For FeAlNi, peaks ascribed to NiO (JCPDS 75-0197) and γ-$Fe_2O_3$ are visible while those of α-$Fe_2O_3$ (JCPDS 79-1741) are obscurely observed. The reflections of $NiAl_2O_4$ and $FeAl_2O_4$ can not be ruled out and this implies that these generated spinel oxides compounds are highly dispersed over the bulk. Particles sizes estimated by Scherer equation shows the nanosized features of the FeAlLa and FeAlZn while the aggregation of FeMgZn and FeAlNi particles implies that the solid has large sizes.

Chemical analyses by ICP-OES results show that the obtained oxides composition is close to that predicted theoretically and corresponding to 68 wt % of $Me_3$ whereas 16 wt % of each $Me_1$ or $Me_2$ specie. If one considers all oxides having or $Me_1Me_2Me_3$ general formulae. The percentage of the elements matches well with the calculated values.

Nitrogen sorption isotherms show that FeAlLa, FeAlZn and FeAlNi catalysts have type IV isotherms with the hysteresis loop between $H_2$ and $H_3$ (Fig.2), which is typical of mesoporous solids.

Fig.2

FeMgZn is an exception, since its isotherm has a type II feature sorption curve. The specific surface area ($Sg_{BET}$) and pore volume (Vp) of FeAlLa are the greatest, among the oxides studied ($Sg_{BET}$=70 $m^2.g^{-1}$; Vp =0.10 $cm^3.g^{-1}$; Dp =39 Å), as illustrated in Table 1. This might be due to their oxides uniformly dispersed as nanocrystallites that are not observed by XRD. FeMgZn catalyst has a rather low surface area (ca. 46 $m^2\ g^{-1}$) and the other textural parameters such as Vp of ca. 0.10 $cm^3.g^{-1}$ and pore diameter of 11Å as well indicate that this solid is microporous and possesses larger particles sizes. Furthermore, pore diameters of FeAlZn and FeAlNi are reasonably large and both $Sg_{BET}$ and pore volumes slightly decreased.

The differences among the $Sg_{BET}$ of the solids are not significant rendering it very suitable surface area for solid obtained by sol-gel method [21,24]. The particles sizes measured by XRD follows the same trends of the textural parameters values and thereby, sintering effects during the calcination process could reduce the textural properties of FeAlZn and FeMgZn. This is in line with their particles sizes values of 16 e 44 nm, respectively, which are measured by XRD.

SEM-EDX images of the solids are illustrated in Fig.3. The morphology of FeAlLa (Fig.3$a_1$,

$a_2$) exhibits a platelet of LaAl-containing phases (e.g., $La_2O_3$-$Al_2O_3$, $La_2O_3$ or $LaAlO_3$ or yet γ- $Al_2O_3$), in which the γ- $Fe_2O_3$ nanoparticles are mostly dispersed. This result indicates that FeAlLa appears to be composed of small particles of iron with the size of ca. 10–20 nm and the mean particle size of thirty nanoparticles is about 15 nm. This is further confirmed by EDX analysis that displays the uniform dispersion of iron nanoparticles on La-Al surface (Fig.3a), which is consistent with the XRD and textural properties results.

On the other hand, the morphology of FeAlNi is markedly different from other solids. Plate-like crystallites are clearly visible (Fig. $3b_1$, $b_2$). The crystallites are believed to be composed of α-$Fe_2O_3$,γ-$Fe_2O_3$ and γ-$Al_2O_3$, as suggested by EDX analyses. The increased magnification to examine the plates shows that homogeneously dispersed particles NiO are on their surfaces. These results are in line with XRD measurements.

Fig.3

SEM-EDX micrographs of FeAlZn reveals a well-formed thin plate-like crystals with sharp edges (Fig.$3c_1$, $c_2$), which are indicative of α-$Fe_2O_3$ or γ-$Fe_2O_3$ and γ-$Al_2O_3$ presence. The existence of some of these phases is suggested by XRD. Additionally, it is clearly observed that finely dispersed ZnO crystallites are superposed in the platelet with the size of ca. 100 nm, in line with XRD analysis. These features are associated with the elevated textural properties of the solid. In addition, a little amount of carbon from the aluminum precursor was found on the Al-containing samples.

From Fig $3d_1$ and $d_2$, it can be seen that FeMgZn is formed by a little agglomeration of particles which are superposed in a platelet. It consists of rather heterogeneous large spherical-like particles with a mean size of 50 nm. These results are consistent with the crystallite size included in Table 1, which are obtained from XRD. They are also in agreement with the previous $N_2$ physisorption results that show the lowest textural properties for FeMgZn. Additional EDX analysis confirms the non-uniform distribution of MgO, ZnO and γ-$Fe_2O_3$ in some regions.

*3.1.2. TPR analyses*

TPR curves are performed to know the reducibility of the ternary oxides catalysts, as shown in Fig. 4.

Fig.4

The curves show two major peaks with maxima at low-temperature centered at around 811K and a high-temperature reduction peak at 920K, as for FeMgZn. It should be assumed that TPR profiles of α-$Fe_2O_3$ and γ-$Fe_2O_3$ relates a first reduction process of $Fe^{3+}$ to $Fe^{2+}$ at around 673K whereas a second peak at about 723K is ascribed to the reduction of $Fe^{2+}$ to metallic Fe [9,21]. Furthermore, pure ZnO and MgO do not reduce at temperatures as low as 1073K [25,26]. As the temperatures of reduction takes place at higher temperatures than those of the literature, the reduction of the iron species could be delayed due to a synergic interaction between iron, magnesium and zinc favoring the redox properties of the material. Another possibility is the interaction between surface iron and MgO and ZnO species forming other compounds in a reduction environment[27]. Besides, a third reduction peak up to 1073K is suggested by TPR curve of FeMgZn. This curve could be attributed to the direct reduction of finely dispersed $MgFe_2O_4$ or $ZnFe_2O_4$ phases; these species show elevated temperatures of reduction by comparing with their bulk counterparts because they are strongly interacting with the support[28,29].

Since γ-$Al_2O_3$, $La_2O_3$, $LaAlO_3$ or $LaAl_{12}O_{19}$ or even $Al_2O_3$–$La_2O_3$ phases do not exhibit reduction peaks at temperatures as low as 1273K, the aforesaid reduction peaks of FeAlLa are associated to the finely dispersed iron oxide reduction on $Al_2O_3$ and/or $La_2O_3$ matrix. The latter enables the difficulty of iron oxide reduction in the catalyst and, thus, decreasing its degree of reduction, compared to FeMgZn.

TPR profile of FeAlZn exhibits an asymmetric peak at ca.680K, which can attributed to the reduction of γ-$Fe_2O_3$ to $Fe_3O_4$. A broad peak in a much wide range from 440 to 943K consists of two components with maxima at ca. 766K and ca. 877K and corresponds to the reduction of $Fe^{2+}$ to $Fe^{o}$ as well. Regarding to this point, it should be emphasized that the reduction of magnetite to metallic iron is affected by the ZnO presence probably due to FeO (wustite) formation[9] while $FeAl_2O_4$ reduction does not occur in concomitance with that of other iron or zinc species.

TPR profile of FeAlNi obviously displays that the reduction peaks of iron species shifts to the higher temperature and exhibits a remarkable broadening of the hydrogen uptake peak due to the formation of reduced metallic iron reduction over nickel aluminate of iron aluminate supports. According to the findings, both iron and nickel aluminate are formed by a solid-state reaction between γ-$Al_2O_3$ and iron or nickel counterparts under moderate temperatures

and oxidative environments[30-33].Typically, pure NiO is characterized by a single TPR peak at 573 and 673K[34-36]. In addition, the peaks position of water formation is not visible over all solids due to the detector limitation. Combing with the XRD results, the latter peak is not visible since it can be mainly dispersed in the solid matrix, as nanoparticles.

*3.2. Catalytic results in the dehydrogenation of ethylbenzene in the presence (absence) of $CO_2$*

The catalytic performance is evaluated by the dehydrogenation of ethylbenzene to styrene over various catalysts. Blank runs provided almost negligible conversion after 5 hours of reaction in the absence of $CO_2$ while its presence gave 2% of conversion.

Fig.5a show the overall conversion and selectivity obtained in 5h of reaction, when $CO_2$ is co-feed in the reaction.

Fig.5

The conversions are high (e.g., up to 10%) in 1h of reaction over all solids. A possible reason for this performance is the cracking of ethylbenzene molecules due to thermal effects at the beginning of the reaction [9,21]. The behavior of solids follows distinct trends as the reaction proceeds. FeAlNi retains 10% of conversion along of the reaction time whereas FeMgZn does not display significant catalytic activity in the same testing period and its conversion gradually decreases with stabilization at 6% in the steady state (Table 1).

Judging from the fact that FeAlNi and FeMgZn possesses the same active $Fe^{3+}$/ $Fe^{2+}$ sites from $\gamma$-$Fe_2O_3$ and their textural properties (Table 1) are closer, the catalytic behavior can be rationally explained by the presence of a their promoters. The findings [31, 32] proposed a mixed acid–basic and reduction–oxidation mechanism for the reaction. There is a formation of $\pi$-adsorbed intermediate on $Fe^{3+}$, which is a Lewis acid center obtained from $\alpha$-$Fe_2O_3$. This step is followed by elimination of two hydrogen ions from two C–H ethylic groups on basic centers; the subsequent electron transfer to $Fe^{3+}$ results in the styrene and $H_2$ production. Bonfim *et al.* reported that [33], bulk Fe-containing ZnO oxides are seen as active phase for ethylbenzene conversion in the presence of steam because of the interaction between the acidic ZnO and $\alpha$-$Fe_2O_3$ forming $ZnFe_2O_4$. Nevertheless, the activity decreases significantly with $Zn^{2+}$ sites in iron-based catalysts in the dehydrogenation of ethylbenzene in

He atmosphere [32] due to the easy reduction of iron species. The same fact can be probably attributed to the deactivation behavior of FeAlZn.

However, using NiO as promoter, FeAlNi activity is not changed significantly, suggesting that the active $Fe^{3+}$ is not reducible enough and the $Fe^{3+}/Fe^{2+}$ reduction–oxidation couple is stabilized on the catalysts (shown by TPR). Whereas $Ni^{2+}$ is reduced to $Ni^{o}$ acting as active sites by increasing the occurrence of side reactions such as ethylbenzene cracking[34,36]. In line, selectivity of styrene over FeMgZn reaches 99 % while FeAlNi production of styrene is only 2% (Fig. 5b). By-products such as toluene, benzene, aromatics, methane and other light products are also found over FeAlNi indicating the predominance of ethylbenzene cracking and condensation reactions as well as Boudouard reaction over $Ni^{o}$ sites[34]. For a comparison purpose, a binary FeCo catalyst prepared by co-precipitation method[35] is also used as catalysts obtaining ca. 5 % of conversion and ca. 9% of styrene selectivity. According to our previous work[36], both $Co^{o}$ and $Ni^{o}$ sites are indispensible elements for coking.

The catalytic reaction rate depends strongly on the dispersion degree of active components. As FeAlZn and FeAlLa possesses $Fe^{3+}$ well dispersed in their large surface (XRD and textural properties) and the results depicted in Fig.5 show that high conversions are achieved at relatively low reaction time (typically under 30 minutes). The conversions over the these solids decrease monotonically and a maximum of ca. 30% is observed for FeAlZn while FeAlLa conversion is about 20% in 4h of reaction, being styrene the main product. Nevertheless, no aimed 100% of styrene is obtained entirely over FeAlLa in 5h and styrene conversion falls simultaneously to 17%. A rational reason for explaining these results above is that, the dispersed nanoparticles expose terrace, corner and edge atoms, and also step atoms, as observed for Fe-based solids obtained by the same preparation method[37]. These types of defects may contribute to increase the ethylbenzene adsorption on $Fe^{3+}$; this action is not observed on $La^{3+}$ or $Al^{3+}$ sites, instead. As the active species containing $Fe^{3+}$ are consumed, conversion is decreased and parallel reaction of ethylbenzene conversion to benzene, ethylene and methane and others accounts for the slight low selectivity over FeAlLa compared to FeAlZn.

Best results are achieved over FeAlZn in reason of the $FeAl_2O_4$ active phase formation, which could be stabilized by ZnO as textural and structural promoter of iron species[33], This catalyst exhibits better results in ODH reaction as compared to FeCo and FeNi, whose the

active phases are $CoFe_2O_4$ and $NiFe_2O_4$ spinel oxides [34]. The latter phases are not selective to styrene and thus, stability is restricted to 2h of reaction. Another factor may be occurrence of parallel RGWS reaction increasing the $CO_2$ conversion at expense of ethylbenzene dehydrogenation, in some cases. This was confirmed later by the modeling and experimental essay of RWGS reaction studies with FeAlNi and FeCo catalysts.

It is important to say that $CO_2$ is reactive enough to be converted on metallic $Ni^o$ sites formed during the reaction on FeAlNi. Whereas MgO adsorption ability for $CO_2$ is rather than the other elements[38] and the reason for this behavior is believed to be due to the presence of either MgO or $MgAl_2O_4$ on FeMgZn, as stated before. For FaAlZn, the ability of Zn sites in converting $CO_2$ can be quite low [39] and thus, a poor $CO_2$ conversion is expected. In case of FeAlLa, lanthanum carbonates can be formed by adsorption of $CO_2$[40] and it can justify the catalytic performance of the solid.

As it can be seen in Table 2, the catalytic performance is significantly affected in the absence of $CO_2$, i.e, DH reaction. The catalytic runs are performed far from equilibrium. When the $CO_2$ is co-feeding the reaction, an enhancement of the EB conversion to 20% is obtained over FeAlNi while the conversion over FeMgZn is about 9% in 5h of time on stream. The deactivation of FeAlNi observed in the ODH reaction (Fig. 5a) is probably due to the reduction of Ni particles by the products $H_2$ and CO in RGWS reaction.

Catalytic performance in the absence of $CO_2$ (Table 2) displays twice as little as that of the parent solids used in the presence of the gas (Table 1). However, no general trend or correlation among iron dispersion, promoter nature and activity can be drawn from EB conversion data. From these results, it can be concluded that simple ethylbenzene dehydrogenation (DH reaction) occurrence is limited in the absence of the mild oxidant due to the reduction of the active iron phase. Also, it appears that the styrene product is not stable in the absence of $CO_2$ and reacts with loss of its selectivity. This will be further investigated over the most active solids.

*3.2.1 Characterization of spent solids*

Raman measurements of the spent solids are performed to describe the structural features of the solids and confirm the existence of carbonaceous deposits after being tested in the reaction (Fig.6).

Fig.6

FeAlLa exhibits two broad bands at around 1345 and 1620 $cm^{-1}$, which are attributed to the D and G bands, respectively; these bands are associated with the deposition of carbonaceous species on solid surface. The D band is ascribed to the defects in the structure or disordered carbons species whereas the G one is originated from the in-plane C–C bond stretching of more ordered graphitized carbon[1]. Most probably, some well dispersed iron nanoparticles of FeAlLa are more prone to be reduced during the reaction and thus, forming metallic iron due to hydrogen presence. Assuming that coking formation is inevitable under the aforesaid conditions, the reason for a lower activity decay of the FeAlLa could be a higher resistance against a fully reduction of the nanoparticles and leaching of the coking by oxi lanthanum carbonate species formed by $CO_2$ from the solid surface [41]. More interestingly, Table 2 shows textural properties of spent FeAlLa is little affected after the reaction, as compared with the fresh solid in Table 1.

In case of FeAlNi, shifting of D and G bands to higher wavenumbers is also observed, as compared to the FeAlLa, especially D band displays a 180 $cm^{-1}$ red-shift. Raman results are in reasonably harmony with those abovementioned catalytic results that suggested the deactivation of this solid owing to ethylbenzene cracking. This is in a good agreement with that report of Menezes[5] that illustrated the deactivation of Fe-based catalysts induced by metallic nickel species which provides the cracking of ethylbenzene molecule to form carbon on solid surface. These results could not be explained without taking into account the damage of the solid surface. As shown in Table 2, the values of the textural properties of the solids decreases significantly compared to the fresh solid, in reason of coking on solid surface.

Investigating the Raman spectrum of FeMgZn more closely, it can be found only one band, namely D one. It implies that the amorphous carbon deposition from ethylbenzene or CO decomposition reactions could be responsible for the poor activity of the solid. A quite satisfactory relationship between Raman results and surface properties is evidenced in Table 2. The low textural properties of the FeMgZn can be ascribed to the much more amorphous carbon deposition on pores and/or solid surface.

No carbon bands are observed for FeAlZn, which is assumed to be due to resistance to coking of the solid. This interpretation is reasonable if the textual properties is still kept for the spent solid (Table 2) . It can be assumed that FeAlZn is a stable catalyst for the reaction.

*3.2.2. Kinetic Constant and RWGS reaction rate determinations*

Using the $C^{++}$ programming tool, the effect of temperature on the RGWS reaction rate is performed with the $CO_2/H_2$ of 1 at 10 bar (Table 3 and Table 4). Not surprisingly, at different operating temperatures (from 400 to 1050K), the results show that the non-catalyzed reaction is favored by increasing the temperatures. However, temperatures superior to 850K significantly slow down $k_{RWGS}$ due to thermodynamic limitations of the process at elevated temperatures (Table 3). Therefore, side reactions such as CO dissociation into $CO_2$ and its further conversion to coking (reaction IV) prevails over the RGWS reaction at around 1100K. Up to this temperature, the overall process becomes close to the maximum allowed by equilibrium, probably due to the equal velocity of WGS and RWGS reactions (IV).

$$2CO \rightleftharpoons CO_2 + Coke \quad \Delta H°_{298.15K} = -172 \text{ kJ mol}^{-1} \qquad \text{(IV)}$$

From Arrhenius plots used to establish a good set temperature dependent rate parameters, a resultant activation energy parameter of $4.01 \times 10^3$ J.mol$^{-1}$ is obtained in accordance with those found elsewhere[42-45].

Thermodynamic parameters $\Delta_rG^o$ and $\Delta_rH^o$ are -3.2 kJ.mol$^{-1}$ and 42.3 kJ.mol$^{-1}$ , respectively at 823K. These values decrease with increasing the temperature, suggesting that the $CO_2$ hydrogenation is favored at high temperatures, otherwise RGWS side reaction occur in spite the main reaction, under these conditions. According to the DFT-refined microkinetic model studies and mechanistic predictions, WGS reaction proceeds via a carboxyl (COOH) mechanism, whereas RGWS reactionproceeds according to a redox (reaction II) one at moderate temperatures[42,45], in a good agreement with our results.

*3.2.3. Adsorption and desorption constants by varying the temperature*

The $CO_2$ and water adsorption constants (e.g., $K_{CO2}$ and $K_{H2O}$ ) are obtained by means of equations 5 and 6. Plots of predicted adsorption constants as a function of temperature are shown in Fig. 7.

Fig.7

Because of the slight endothermicity of the RWGS reaction, $K_{CO2}$ gradually increases with the temperature increment (Fig.7a). Also, elevated temperatures lead to higher $K_{CO2}$ values than those of $K_{H2O}$ and this is also reflected in their velocity rates. These differences are appreciable at temperatures below to 950K, in which RWGS is thermodynamically favored [43].

Many mathematical models have been developed by investigators to predict the evolution of the effective RGWS reaction on a solid surface and mostly agreed that $CO_2$ adsorption is favored at temperatures lower than 850K, due to mono and bidentade compounds formation with $CO_2$, on the catalyst surface [44].

It has been assumed that when temperatures are superior to 950K, the parameters tends to values close to zero in reason of the difficulty of $CO_2$ to be adsorbed on solid surface. Thus, the $CO_2$ is faster decomposed to carbon monoxide and traces of the effluents are detected in low amounts, resulting in reduced desorption constants.

The influence of the reaction temperature on the $K_{H2O}$ behavior is examined in temperatures ranging from 850 to 1000 K (Fig.7b). The model considering water adsorption gives reasonable results and the main reason is the good capture water at temperatures as low as a 950K. Furthermore, the curves provides reasonable accuracy and a good agreement with the fact that RWGS reaction is favored upon using these conditions, as observed for catalytic runs over Ru and carried out at 850 K[47]. It is interesting to consider the observations above in the light of the recently reported Cu–Fe catalysts tested under the same conditions, which demonstrate the abilities of CO and water to dessorb from Cu–Fe surfaces during steam reforming of methane [19].

Fig. 8 displays the plots of deactivation constants (e.g., $K_{H2Od}$ and $K_{CO2d}$) versus temperature. Of all the models considering a hypothetic surface where CO and $H_2O$ species react[39,42, 48], the curve provides the best fit to corroborate that the deactivation of these entities on solid surface is faster over $CO_2$ than $H_2O$ at temperatures as low as 950K. This result indicates that the reaction is more favorable at temperatures lower than 950K, as reactant molecules of $CO_2$ dispropotionate to form CO and the rate of this reaction is too high compared with other parallel reactions[42,48].

The value of adsorption constant (k`a) is found to be = $7.9 \times 10^{-25}$ $s^{-1}$ at 850 K by using Eq.7-The reaction in this study is more influenced by an increase in the reaction temperature. Besides, the deactivation on the external surface of the catalyst is assisted by $CO_2$ decomposition parallel reaction more than the own $CO_2$ adsorption. Finally, the plots of adsorption constants vs temperature result in an exponential curve, which is regarded as sufficiently good to indicate that temperatures below 950K are adequate to show the $CO_2$ adsorption rate is the determining step of the reaction, which is elevated enough to allow

RWGS parallel reactions. However, $CO_2$ deactivation rate is also enhanced at these temperature conditions. In addition, the model shows a strong tendency to underestimate the conversions at elevated temperatures.

*3.2.4 Effect of the $CO_2/H_2$ on the occurrence of RWGS*

The reverse water gas shift reaction is studied under distinct $CO_2/H_2$ ratios by varying the temperature. RWGS reaction rates is gradually enhanced upon increasing the partial pressure of the reactants (Table 4) due to the shift of equilibrium to form CO and water, as it has already been stressed out in the literature[49,50].

Table 4

Lower $CO_2/H_2$ inferior to 1 corresponds to an increase of the $H_2$ content in the feed and this can favor the competition among the following reactions: WGS (backward reaction I), hydrogenation of $CO_2$ to methanol or ethanol (reactions V-VII), methane formation (reaction VIII), alkenes formation (reactions IX and X) and coking by CO reduction (reaction XI) [25,26]. Moreover, RWGS is not thermodynamically favored under lower $CO_2/H_2$, indicating the kinetic factors prevail over the thermodynamic ones.

$CO_2 + 3H_2 \rightarrow CH_3OH + H_2O$ (V)

$CO_2 + 4H_2 \rightarrow CH_3OH + 2H_2O$ (VI)

$2CO_2 + 6H_2 \rightarrow C_2H_5OH + 3H_2O$ (VII)

$CO_2 + 4H_2 \rightarrow CH_4 + 2H_2O$ (VIII)

$2CO_2 + 7H_2 \rightarrow C_2H_6 + 4H_2O$ (IX)

$3CO_2 + 9H_2 \rightarrow C_3H_6 + 6H_2O$ (X)

$CO_2 + 2H_2 \rightarrow C + 2H_2O$ (XI)

Nevertheless, the rates reach a plateau and a maximum value of $CO_2/H_2$ =1, which tends to be favored due to stoichiometric relations of the RGWS reaction even if elevated conditions are obtained at $CO_2/H_2$ ratios superior to 1. Thereby, reaction rate levels up 1.0 $10^{-19}$ mol.$h^{-1}$ is achieved at $p_{CO2}/p_{H2}$ reaching 1.

A part from the modeling results, RWGS reaction occurrence is preferred at $CO_2/H_2$ molar ratio of 1 and a temperature of 850K.

*3.3. Experimental studies in RWGS over the catalysts studied*

Catalytic runs in the RGWS reaction were carried out over FeAlNi and FeCo (Fig.9), being the latter a reference catalyst. The reaction conditions are the $CO_2/H_2$ molar ratio of 1 temperature of 850K. A detailed description of FeCo reference catalyst and its textural and structural features of the solids have be given in ref. [42].The FeMgZn and FeAlLa catalysts are not actives in the RGWS reaction due to the lack of active sites to catalyze the reaction whereas conversion of FeAlZn shows activity in the first minutes of the reaction and then falls to zero.

Experimental and both experimental and predicted conversion has shows good fit.

Fig. 9

The $CO_2$ conversion of Fe-based catalysts increases rapidly from 0 to 2.5 % at 600 K and thereafter, it appears that best catalytic activity can be attained with 20.3% of conversion at 1400 K (Fig. 9a). Both, the $CO_2$ conversion and CO selectivity do not follow the same trends due to WGS reaction predominance over certain catalysts, as shown in Fig. 9b. Instead, FeAlZn is inactive even at high temperatures. It is well known that Ni in iron-based catalysts promotes the WGS reaction at temperatures as high as 600K due to reaction kinetic control and the catalyst is very active, stable and selective to CO at high temperatures [50-52]. The latter is activated more rapidly, but after few 1h of reaction, it became quickly deactivated due mainly to formation of coke residues on the catalysts along the test. Carbon monoxide selectivity linearly decreases with increasing the temperature ensuring that the catalytic activity for CO decomposition to coking at elevated temperature is likely. This is favored when reduced nickel particles are present as on the surface of support.

Moreover, the inverse relationship between CO selectivity and temperature also suggests that the RWGS endothermic reaction need heat to achieve high $CO_2$ conversion. Since extremely high temperatures are impractical to commercial application of catalysts in RWGS reaction, thermodynamically favorable parallel reactions such as Boudouard (reaction VIII) and methanation (reaction XI) could be likely over FeAlNi catalyst. In case of FeAlZn, the oxidation of iron nanoparticles may be not likely; as consequence, loss of the active sites need for the reaction and thus, CO selectivity is meaningless in the range of temperature studied. The results indicated that the metallic Co nanoparticles are mainly responsible for the

catalytic performance, since the FeCo shows two times higher activity than FeAlNi catalyst. Such an observation hints towards how the reaction conditions (temperature and composition) can affect the catalytic conversion. The results are indeed in excellent agreement with those obtained theoretically.

From these results it can be concluded that FeAlZn is very advantageous in the ethylbenzene conversion in the presence of $CO_2$ to produce styrene, since the coupled reaction and the stability of the dispersed iron active phase makes the occurrence of RGWS reaction effectively reduced.

## 4. Conclusions

The ethylbenzene dehydrogenation in the presence of $CO_2$ (or its absence) was investigated over Fe-based catalysts. Among the various ternary systems studied that containing La and Zn promoters showed best results due to the dispersion of $\alpha$-$Fe_2O_3$ and $\gamma$-$Fe_2O_3$ nanoparticles on their matrix in the presence or absence of $CO_2$. FeAlZn was the most active solid in ODH reaction whereas FeAlNi exhibited the best performance in DH reaction, among the catalyst studied. Catalytic results in the RWGS reaction were performed by means of kinetic modeling and experimental studies. The optimal conditions for RWGS reaction occurrence were at 850 K, using a ratio of $CO_2/H_2$ = 1, which were proved by the experimental results for FeAlNi. The $CO_2$ adsorption constant decreased with increasing the temperature; this factor was responsible for the greatest reaction rate at temperatures close to 850 K, due to $CO_2$ disproportioning reactions occurrences. Although the reaction rate was elevated at high hydrogen and carbon dioxide partial pressures, the $CO_2/H_2$ ratio values lesser than 1 led to the formation of hydrocarbons whereas those superior to the unity gave the $CO_2$ degradation. A $CO_2/H_2$=1 ratio and temperature of 850K were the best condition for RWGS reaction occurrence while ODH one was not favoured under these conditions. From the catalytic results, the FeAlZn showed a poor performance in RGWS reaction compared to that FeAlNi catalystdue to the active phase degradation of the former solid. Thus, FeAlZn is best suited for ethylbenzene dehydrogenation coupled to RGWS and this solid exhibited 30% of ethylbenzene conversion, being entirely selective to styrene.

**Acknowledgments**

We gratefully acknowledge FUNCAP (0011-00206.01.00/09) and CNPq (473568/2012-8) for financial support.The authors are also acknowledged to Central Analítica da UFC for SEM-EDX analyses.

**References**

1. A.L. Pinheiro, A.N. Pinheiro, A. Valentini, J.M. Filho, F.F.d. Sousa, J.R. Sousa, M.G.C.Rocha, P. Bargiela, A.C. Oliveira, Catal. Commun. 2009,**11,** 11–14.

2. J. Li, C. Hu, K. Tong, H. Xiang, Z. Zhu, Z. Hu, RSC Adv., 2014,**4**, 44377-44385.

3. N. R. Shiju, M. Anilkumar, S. P. Gokhale, B. S.Rao,C. V. V. Satyanarayana,Catal. Sci. Technol., 2011,**1**, 1262-1270

4. C. Nederlof, V. Zarubina, I. V. Melián-Cabrera, E. H.J. Heeres,F.Kapteijn, Appl. Catal.A: Gen.2014,**476**, 204–214.

5. I.M. Nogueira, G.Q. Sabadia, A.A. Moreira, J.M. Filho, A.C. Oliveira, , J. Mol. Catal, A: Chem. 2011, **351**,81–92.

6. X.Ye, Y. Yue, C.Miao, Z.Xie, W. Hua,Zi Gao, Green Chem., 2005,**7**, 524-528.

7. C. L. Lima, O. S. Campos, A. C. Oliveira, F. F. de Sousa ,J. M. Filho, P. L. Neto, A.N. Correia, G.Q. Sabadia, I. M. Nogueira, G. S. Pinheiro, A. C. Oliveira, Appl. Catal. A: Gen. 2011,**395**, 53–63.

8. S. Zhang, X.Li, J. Jing, H.Fan, Q. Wang, W. Li,Catal.Commun. 2013,**34**, 5–10.

9. J.C.S. Araujo, F.N.A. Freire, C.B.A. Souza, A.C. Oliveira, A.P. Ayala, A.C. Oliveira, Appl. Catal. A: Gen. 2010,**377**, 55–63.

10. A.J.R. Castro, J. M. Soares, J. M. Filho, A. C. Oliveira, A. Campos, E. R.C. Milet, Fuel,2013,**108**, 740-748.

11. Q. Wang, X. Li, W. Li, J. Feng, Catal. Comm. 50 (2014) 21-24.

12. A. Aouissi, D. Aldhayan, S. Alkathani, Chin.J. Catal. 2012,**33**, 1474-1479.

13 F. F.. de Sousa, H. S.A. de Sousa, A.C. Oliveira,M. C.C. Junior, A. P. Ayala, E. B. Barros, B. C. Viana, J. M. Filho, A. C. Oliveira,Int.J. Hydrogen Energy 2012,**37**, 3201-3212.

14. V. Zarubina, C. Nederlof, B. van der Linden, F. Kapteijn, H.J. Heeres, M. Makkee, I. Melián-Cabrera,J. Mol. Catal. A: Chem. 2014,**381**, 179-187

15. S.Patel, K.K. Pant, Chem. Eng. Sci.2007,**62**, 5425 – 5435.

16. W. M. Haynes, CRC, Handbook of Chemistry and Physics, National Institute of Standards and Technology, Boulder, 2012, 3rd edition, Colorado, USA.

17. J.Erena, I.Sierra, A. T. Aguayo, A. Ateka, M.Olazar, J., Bilbao, Chem. Eng. J. 2011,**174**, 660– 667.

18. C. Hermann, E Quicker, R. Dittmeyer, , J. Membrane Sci. 1997,**136** 161-172.

19. D. C. Carvalho, N. A. Ferreira; J. M. Filho, A. C. Oliveira, O. P. Ferreira, J. M. Soares, , Catal. Today,2014, in Press Doi: 10.1016/j.cattod.2014.08.010.

20. M. Benito, S. Garcıa, P. Ferreira-Aparicio, L. G Serrano, L. Daza, J. Power Sources,2007,**169**, 177–183.

21. A. J. R. Castro, S. P. D. Marques, J. M. Soares, J. M. Filho, G. D. Saraiva, A. C. Oliveira, Chem. Eng. J., 2012,**209**, 345-355.

22. A. Barrera, M. Viniegra, V.H. Lara, P. Bosch-Giral, Catal Commun 2004,**5**, 569–74.

23. G.A. El-Shobaky, A.A. Mostafa, Thermochim. Acta 2003,**408**, 75–84.

24. Y. Lee, K. Jun, J. Park, H. S. Potdar, R. C. Chikate, J. Industrial Eng. Chem.2008,**14**, 38.

25. W. Jianxin, L. Laitao, Catal. Lett., 2008,**126**, 325-332.

26. F. Mirzaei, M. Rezaei, F. Meshkani, Z. Fattah, J. Industrial Eng. Chem, In Press, (2014) doi: 10.1016/j.jiec.2014.03.034.

27. A.E. Palomares, A. Uzcátegui, A. Corma. Catal. Today 2008, **137**,261-266.

28. R. J. Balasamya, B. B. Topea, A. Khurshida, A. A. S. Al-Alia, L. A. Atanda, K. Sagata, M. Asamoto, H. Yahirob, K. Nomurac, T. Sanod, K. Takehiraa, S. S. Al-Khattaf, Appl. Catal. A: Gen. 2011,**398**, 113–122.

29. L. Ma, R. Wua, H. Liua, W. Xua, L. Chenb, S. Chen, Solid State Sci.2011,**13**, 2172-2176.

30. P. H. Bolt, F. H. P. M. Habraken, J. W. Geus, Formation of Nickel, J. solid state chem. 1998,**135**, 59-69.

31. N. Dulamiţă, A. Măicăneanu, D.C. Sayle, M. Stanca, R. Crăciun, M. Olea, C. Afloroaei, A. Fodor, Appl. Catal. A: Gen., 2005, **287**, 9–18.

32. P. Kuśtrowski, L. Chmielarz, A. Rafalska-Łasocha, B. Dudek, A. Pattek-Janczyk, R. Dziembaj,Catal. Commun.2006,**7**,1047-1052

33. H. E. L. Bonfim, A. C. Oliveira, M. C. Rangel, , React. Kinet. Catal. Lett., 2003, **80**, 359-364.

34. R. M. Freire, F. F. de Sousa, A. L. Pinheiro, E. Longhinotti, J. M. Filho, A. C. Oliveira, P. C. Freire, A. P. Ayala, A. C. Oliveira, Appl. Catal. A: Gen,2009, **359**, 165-179.

35. D. C. Carvalho, N. A. Ferreira; J. M. Filho, A. C. Oliveira, O. P. Ferreira, Dry reforming of methane over mixed oxides obtained from thermal decomposition of layered double hydroxides. In: XXII International Materials Research Congress (2013), p. 60.

36. A. H. M. Batista, F. F. Sousa, S. B. Honorato, A.P. Ayala, J. M. Filho, F. W. Sousa, A. N. Pinheiro, J.C.S. Araujo, R. F. Nascimento, A. Valentini, A. C. Oliveira, J. Mol. Catal. A: Chem., 2010, **315**, 86-98.

37. R.A. Van Santen, Accounts Chem. Res., 2008, **42**,57-66.

38. J. Feng, Y. Ding, Y. Guo, X. Li, W. Li , Fuel2013,**109**, 110-115

39. F. Arena, G. Italiano, K.Barbera, S. Bordiga, G. Bonura, L.Spadaro, F. Frusteri, Appl. Catal.A: Gen.2008,**350**, 16-23.

40. D. C. Carvalho, H. S. A. de Souza, J. M. Filho, A. C. Oliveira, A.Campos, E.R.C. Milet, F. F. de Sousa, E. Padron-Hernandez, A.C. Oliveira, Appl. Catal.A: Gen.2014,**473**, 132-145.

41. H. S. A. de Sousa, A. N. da Silva, A. J.R. Castro, A. Campos, J. M. Filho, A. C. Oliveira, Int.J. Hydrogen Energy, 2012,**37**, 12281-12291.

42. M.J.L. Gines, A.J. Marchi, C.R. Apesteguia, Appl. Catal. A: Gen.1997,**154**, 155-171.

43. S. P. Naika, T. Ryub, V. Buib, J. D. Millerb, N. B. Drinnanc, W. Zmierczak,Chem. Eng. J. 2011,**167**, 362-368

44. F. Arena, G.Mezzatesta, G. Zafarana, G. Trunfio, F. Frusteri, L. Spadaro J. Catal.2013,**300**, 141-151.

45. M. Maestri, K.Reuter, Chem. Eng. Sci.2012,**74**,296–299.

46. H. Watanabe, M. Otaka, Fuel.2006, **12-13**, 1935–1943.

47. M.A. Soria, C. Mateos-Pedrero, A. Guerrero-Ruiz, I. Rodrıguez-Ramos, Int.J. Hydrogen Energy,2011,**36**, 15212-15220.

48. D.G. Avraam, T.I. Halkides, D.K. Liguras, O.A. Bereketidou, M.A. Goula, Int.J. Hydrogen Energy2010,**35**, 9818-9827.

49. S.Saeidi, N.A. S.Amin, M.R. Rahimpour, Journal of $CO_2$ Utilization, 2014, **5**, 6-81

50. M.Suk Lee, J.Y. Lee, D.-W. Lee, D. J. Moon,K.Y. Lee, Int.J. Hydrogen Energy 2012,**37**, 11218-11226.

51. F Malherbe, C Forano, B Sharma, M.P Atkins, J.P Besse,Appl. Clay. Sci. 1998,**13**, 381-399

52. G. Pekridis, K. Kalimeri, N. Kaklidis, E. Vakouftsi, E.F. Iliopoulou, C. Athanasiou, G.E. Marnellos, Catal. Today, 2007, **127**, 337–346.

| | |
|---|---|
| $CO.S$ | active sites occupied by oxygen atom |
| $C_T$ | total amount of active sites occupied |
| $Cv$ | active surface sites available per catalyst mass |
| $\Delta H_{CO2}$ | $CO_2$ enthalpy, kJ $mol^{-1}$ |
| $\Delta H_{H2O}$ | water enthalpy, kJ $mol^{-1}$ |
| $f_{CO2}$ | fugacity of $CO_2$, bar |
| $f_{H2O}$ | fugacity of $H_2O$, bar |
| $K_{CO}$ | ratio between the adsorption and desorption constants of CO |
| $K_{CO2}$ | ratio between the adsorption and desorption constants of $CO_2$ |
| $K_{H2O}$ | ratio between the adsorption and desorption constants of $H_2O$ |
| $K^*_{H2O}$ | Capacity for $H_2O$ adsorption at reference temperature (548 K), $bar^{-1}$ |
| $K^*_{CO2}$ | Capacity for $CO_2$ adsorption at reference temperature (548 K ), $bar^{-1}$ |
| $k'_a$ | kinetics constant for adsorption (Eq 9) |
| $k'_d$ | kinetics constant for desorption (Eq 10) |
| $k_a$ | kinetic constant for adsorption without products influence, $s^{-1}$ |
| $k_d$ | kinetic constant for desorption without products influence, $s^{-1}$ |
| $K_{H2O}$ | kinetic constant of velocity for $H_2O$ |
| $k_{CO2}$ | kinetic constant of velocity for $CO_2$ |
| $P_{CO}$ | partial pressure of CO, bar. |
| $P_{CO2}$ | partial pressure of $CO_2$, bar |
| $P_{H2}$ | partial pressure of $H_2$, bar |
| $P_{H2O}$ | partial pressure of $H_2O$, bar. |
| $-r'CO_2$ | rate of carbon dioxide consumed (Eq 1) |
| $r'H_2O$ | rate of water produced (Eq 2) |
| $r_{RWGS}$ | velocity rate of *RWGS* (Eq 11) |
| $\theta$ | attenuation of the velocity rate by $CO_2$ and water adsorption (Eq 7) |
| $\theta_\delta$ | attenuation of the velocity rate by $CO_2$ and water desorption (Eq 8) |

**Figures**

**Fig. 1.** XRD patterns of the fresh catalysts studied. The solids were calcined at 873 K under air flow.

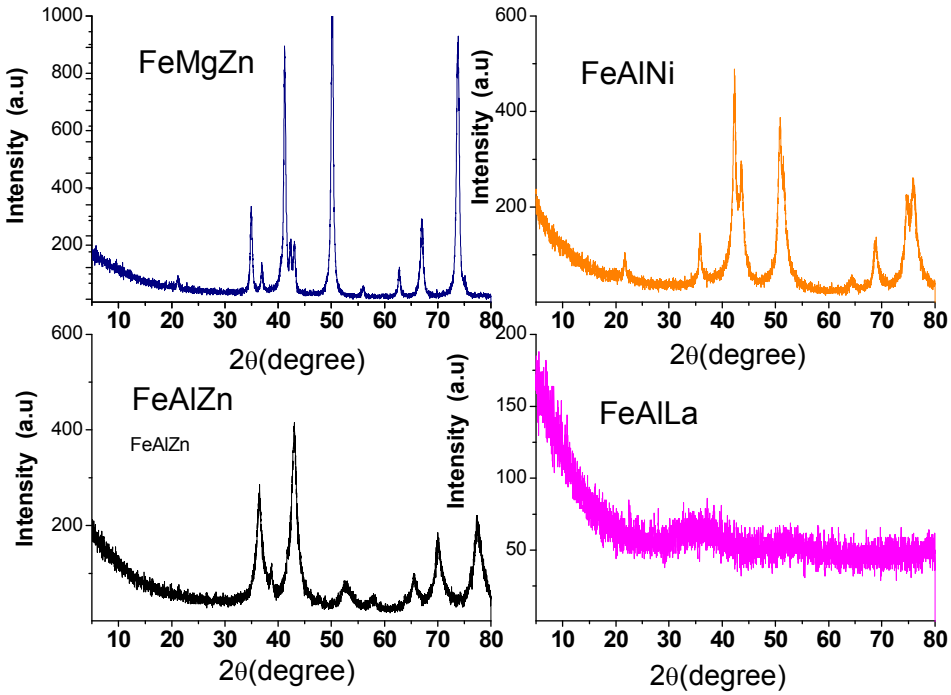

**Fig.2.** (a) Nitrogen adsorption isotherms of the fresh catalysts. (b) The corresponding BJH pore size distribution of the solids.

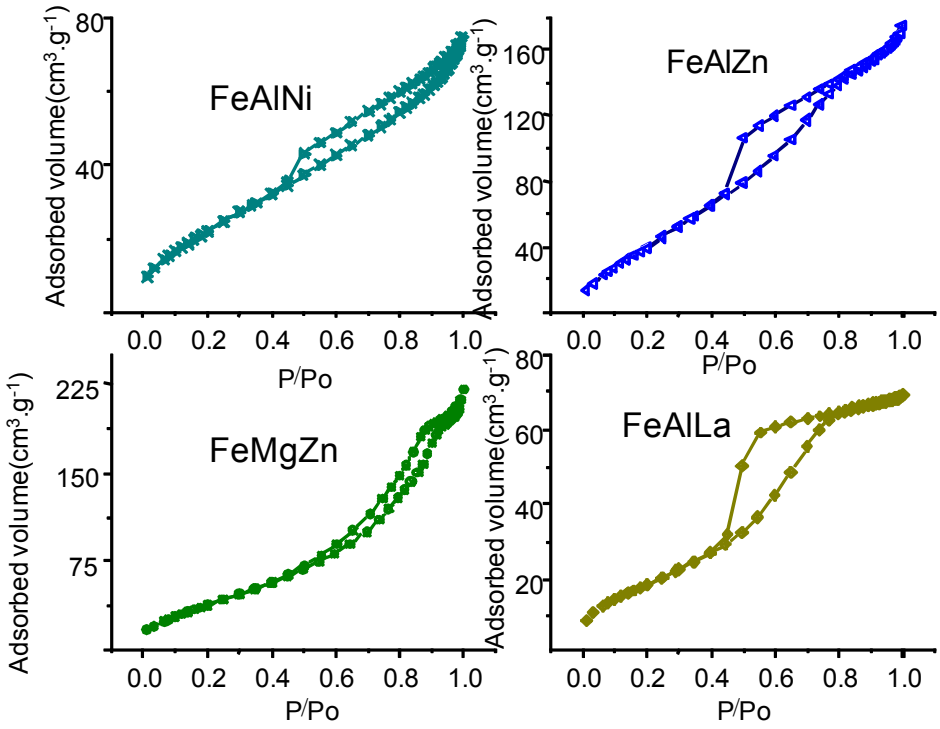


(a)

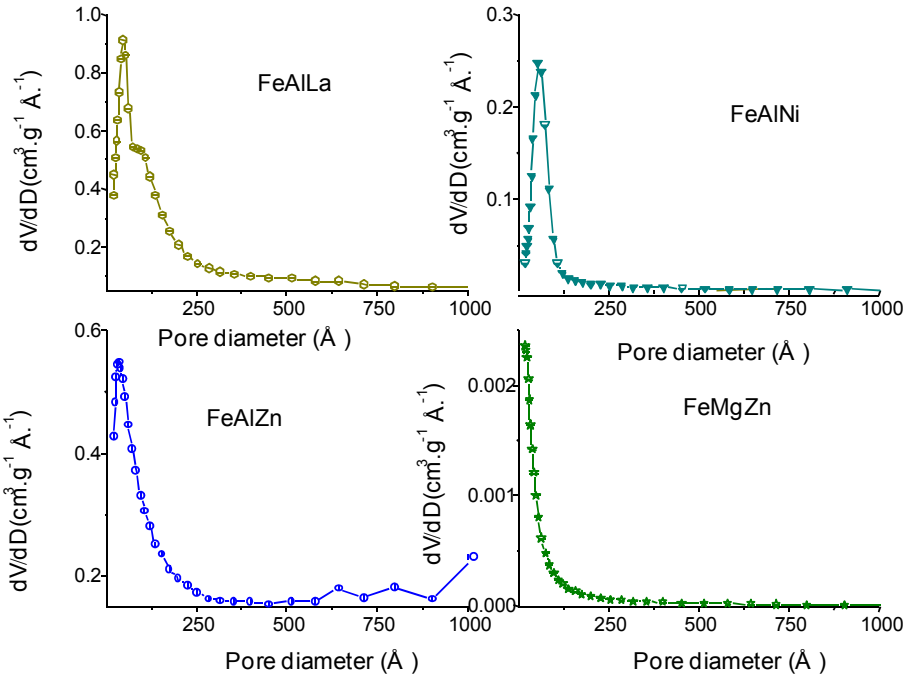


(b)

**Fig.3.**SEM images of the fresh catalysts: FeAlLa ($a_1$ and $a_2$), FeAlNi($b_1$ and $b_2$), FeAlZn($c_1$ and $c_2$) and FeMgZn($d_1$ and $d_2$). The EDX images are represented by $a_3$, $b_3$, $c_3$ and $d_3$, respectively for FeAlLa, FeAlNi, FeAlZn and FeMgZn catalysts.

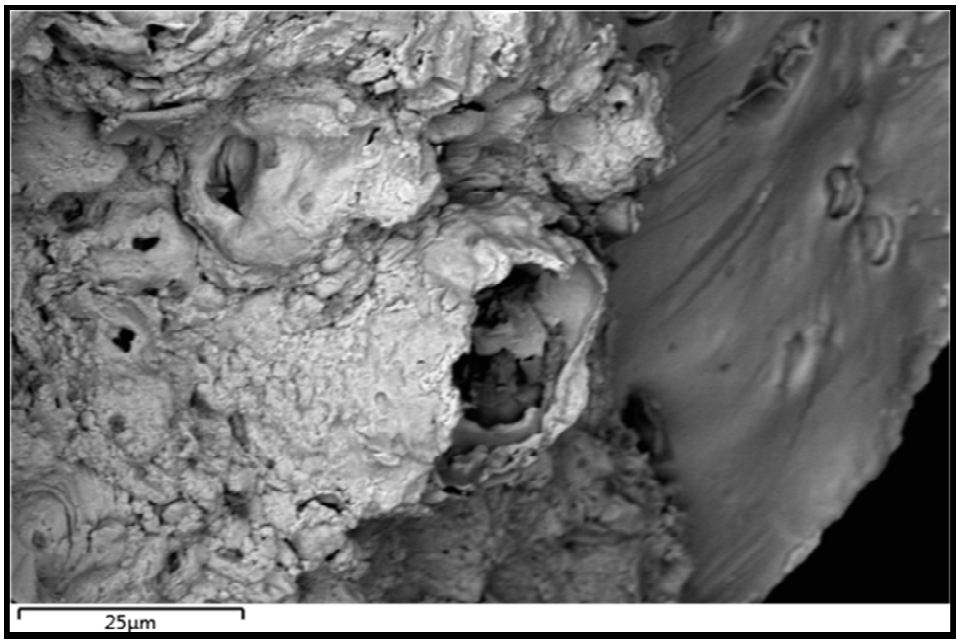


($a_1$)

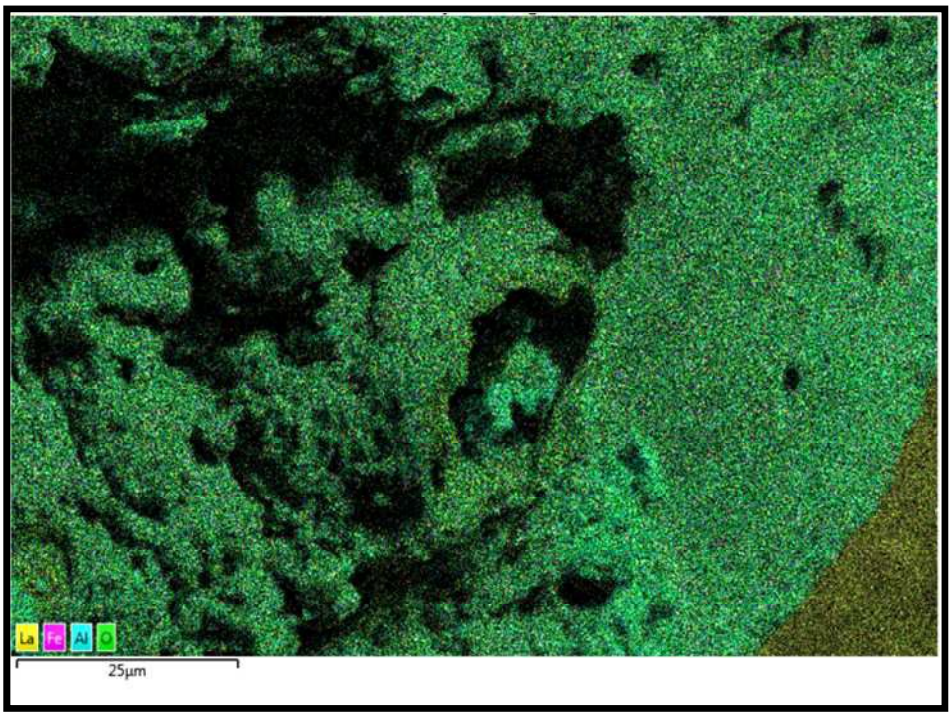


($a_2$)

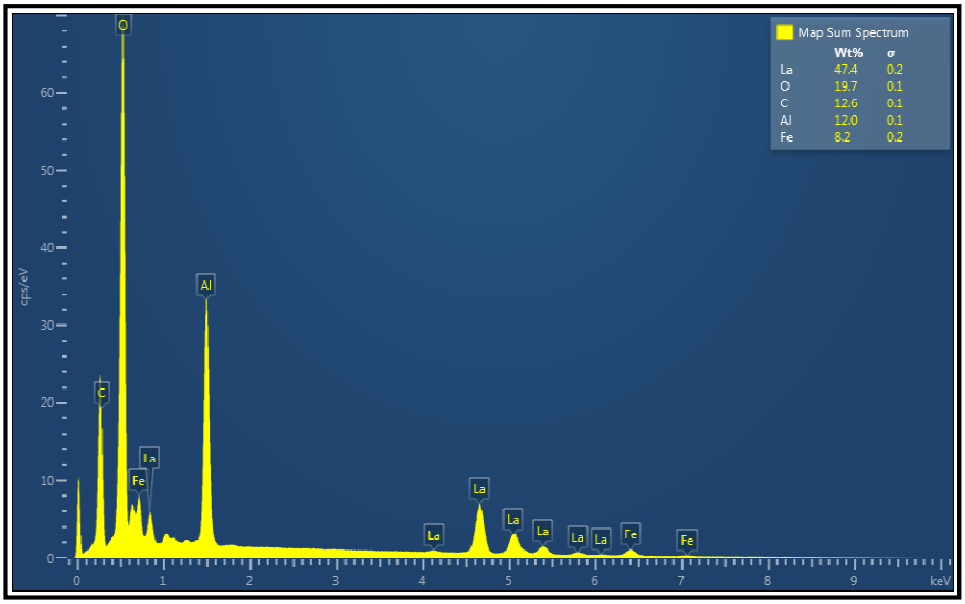


($a_3$)

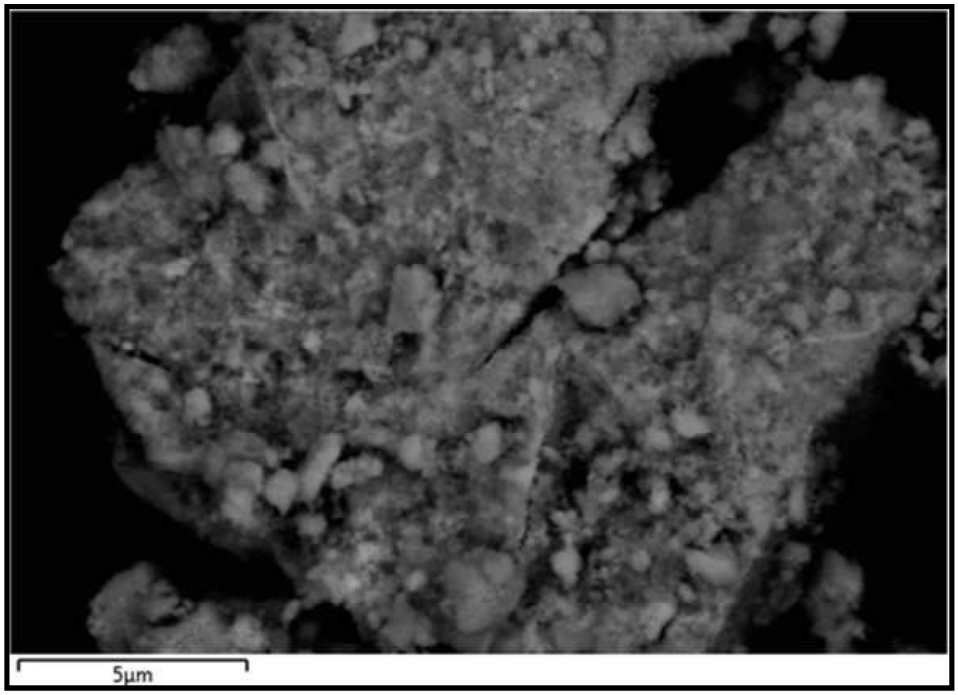


($b_1$)

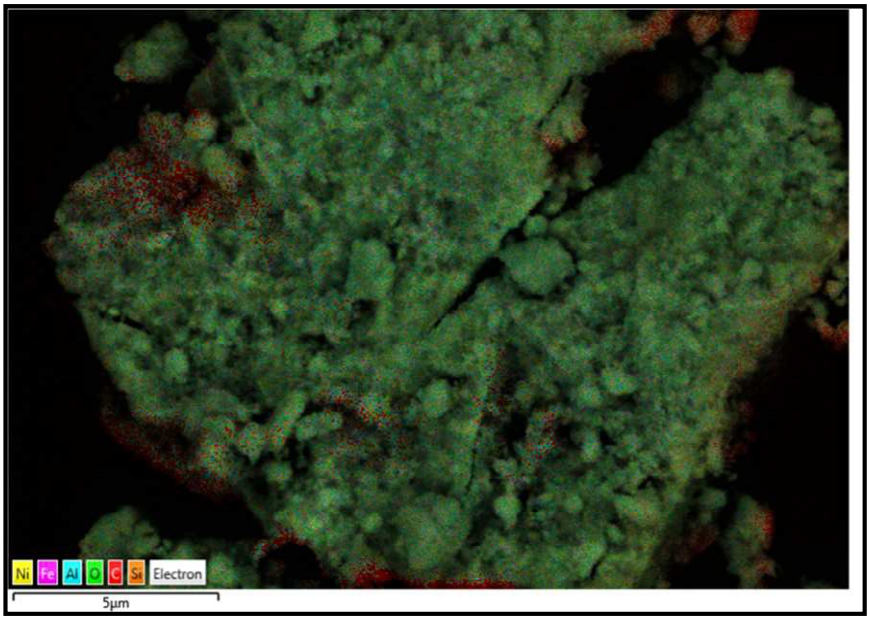


($b_2$)

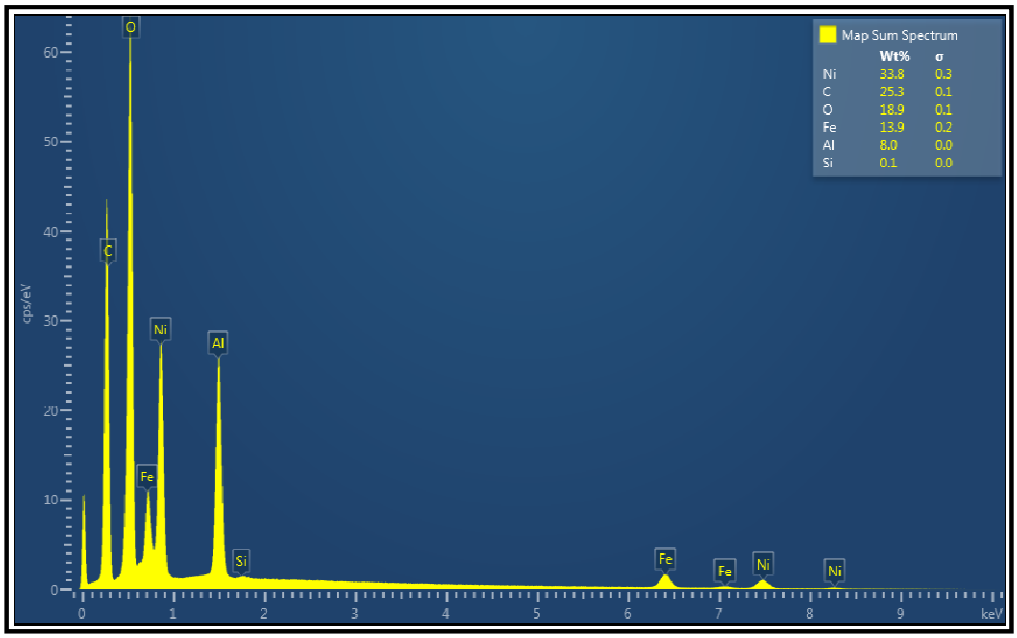


($b_3$)

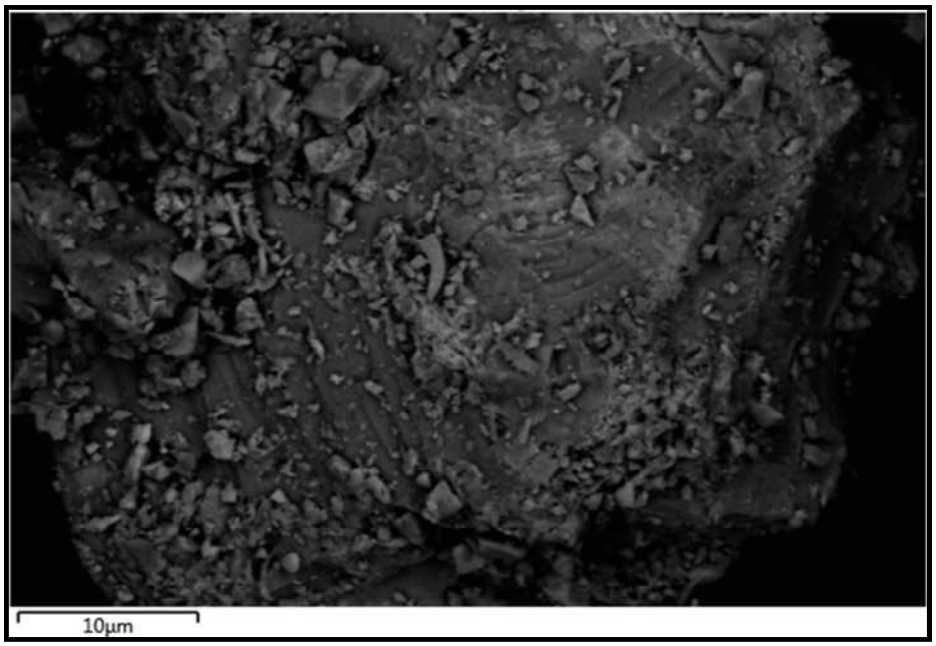


($c_1$)


(c$_2$)

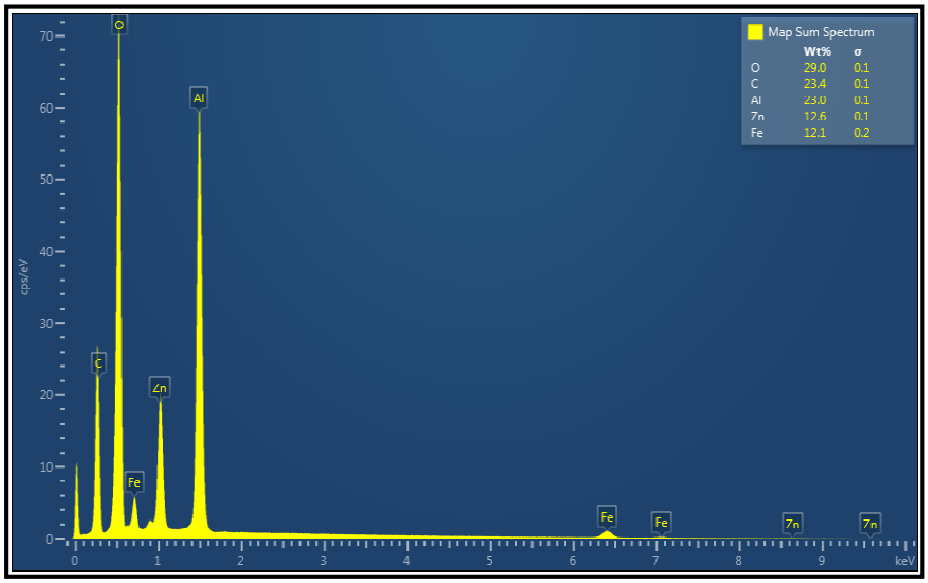


(c$_3$)

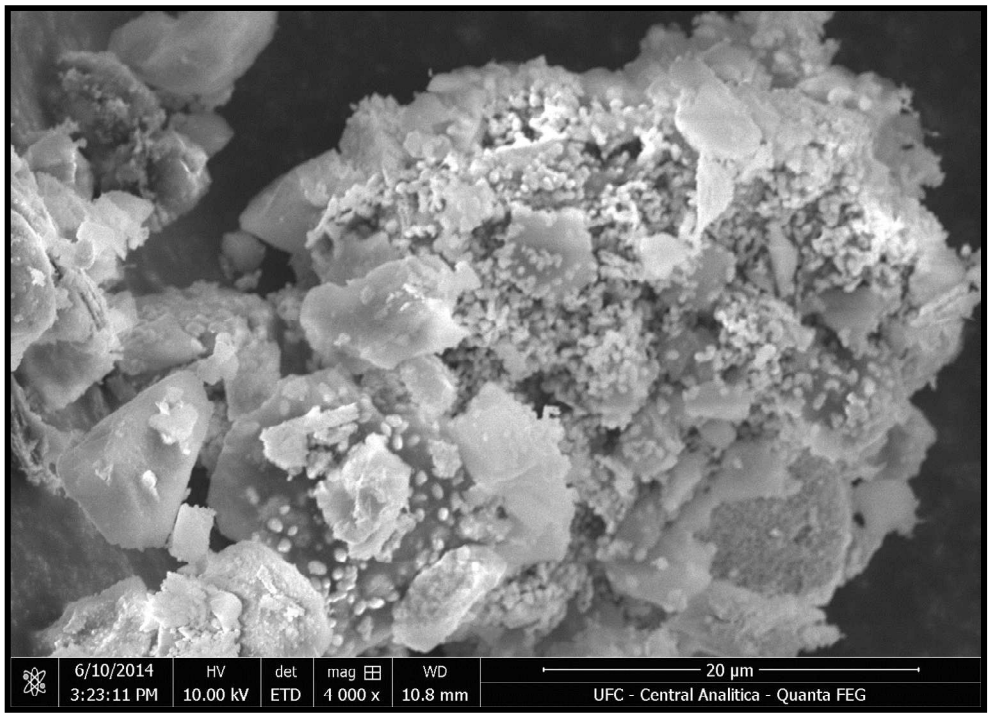


($d_1$)

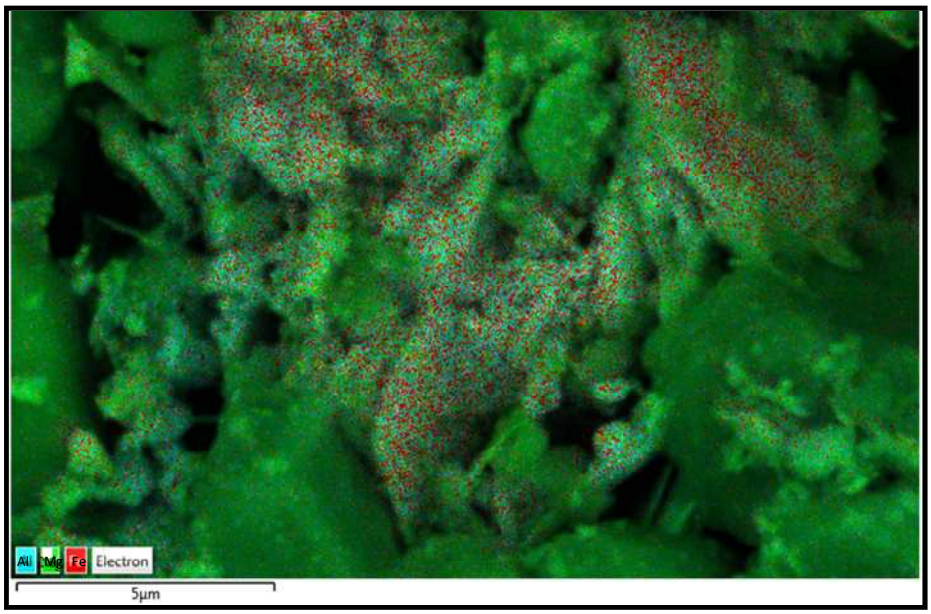


($d_2$)

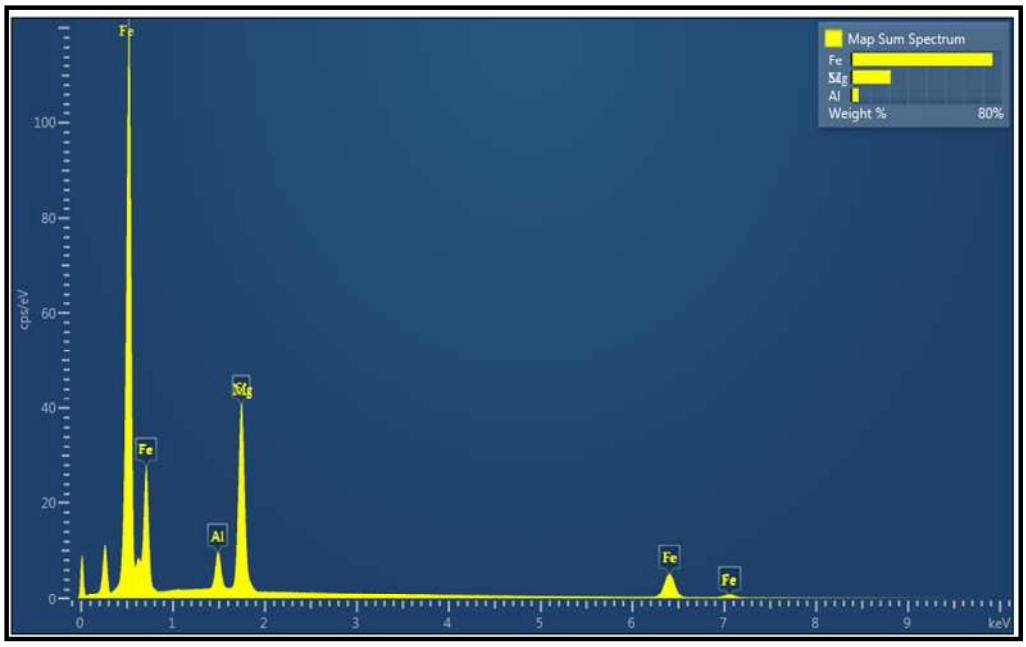


($d_3$)

**Fig.4**. TPR profiles of the fresh catalysts.

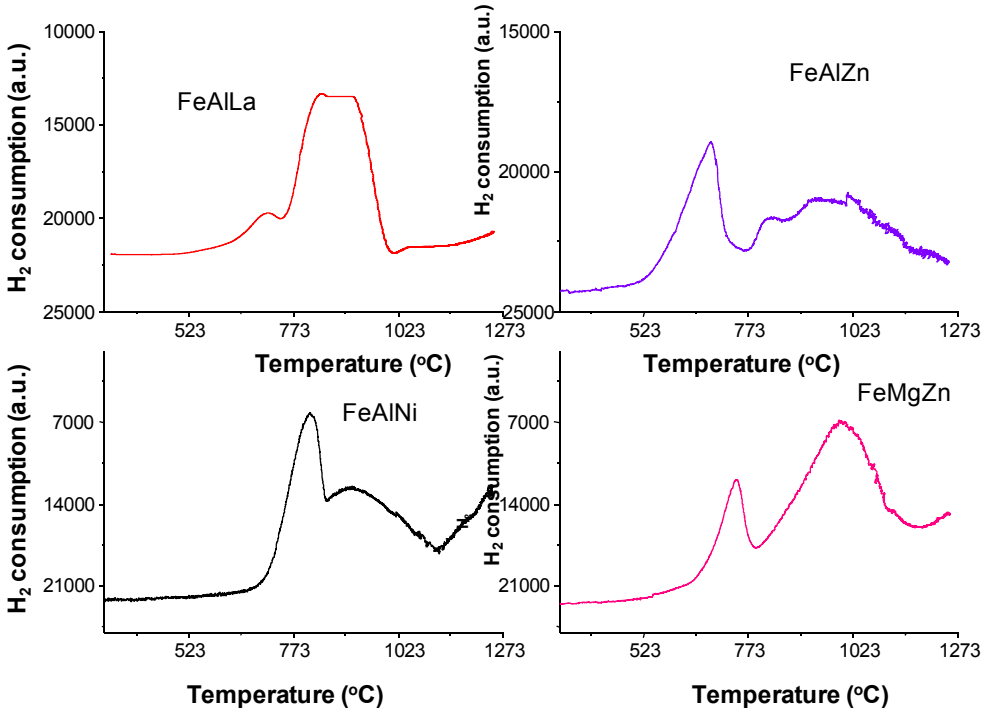

**Fig.5.** (a) Catalytic results in the dehydrogenation of EB in the presence of $CO_2$.The open symbols represents the conversion whereas the close ones are the selectivities to styrene. (b) Overall selectivity to the products formed during the reaction in 5h. The reaction was performed under atmospheric pressure at 823 K and $CO_2$ /EB molar ratio of 30.

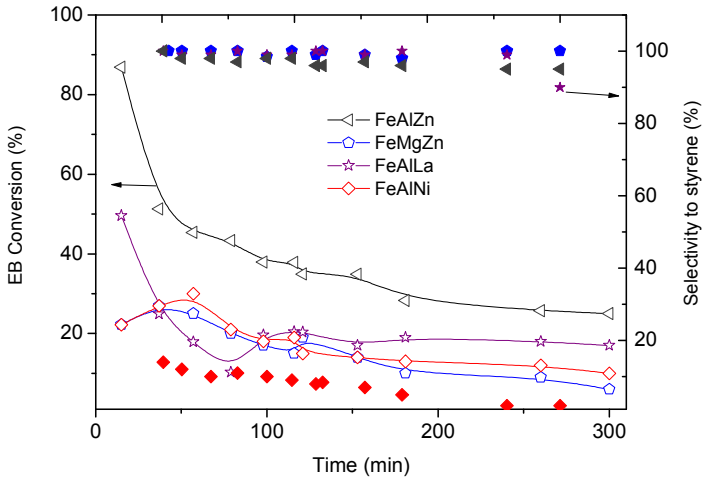


(a)

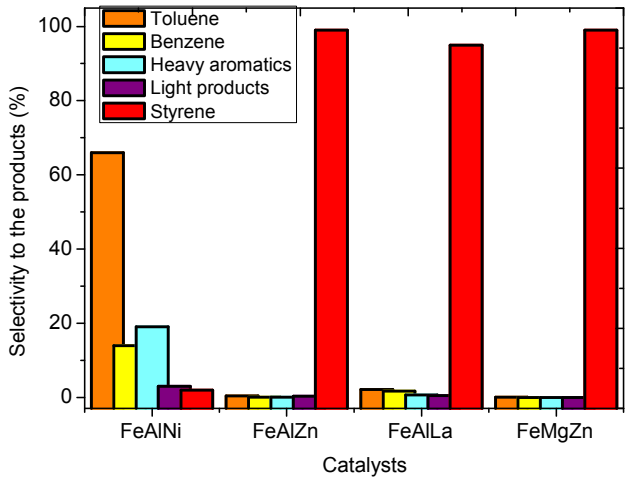


(b)

**Fig.6.** Raman measurements for spent catalysts. The solids were used in the reaction under atmospheric pressure at 823 K and $CO_2$ /EB molar ratio of 30 during 5h.

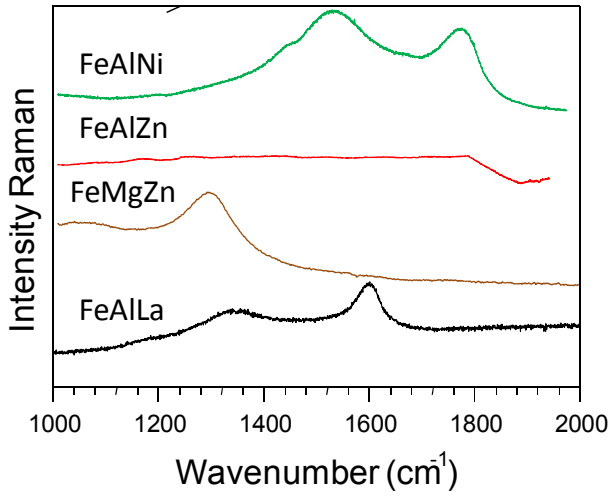


**Fig.7.** (a) $CO_2$ adsorption constant at various temperatures obtained for a hypothetic catalyst surface. (b) Water adsorption constant in function of the temperature for the aforesaid hypothetic catalyst surface.

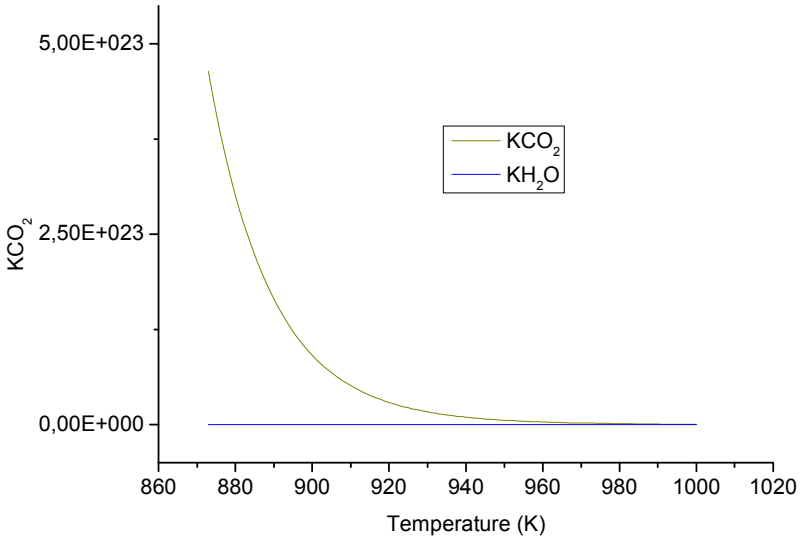


(a)

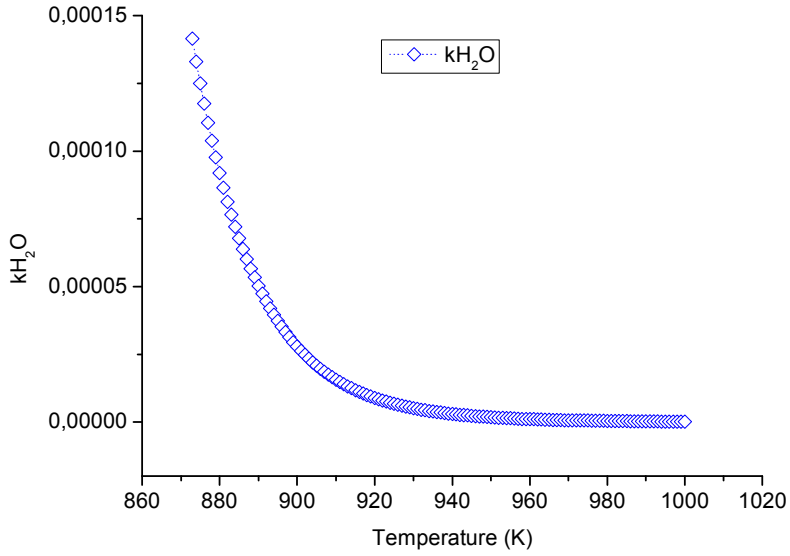


(b)

**Fig.8.** (a) Deactivation constants of $CO_2$ obtained for a hypothetic catalyst.(a) Deactivation constants of water for a hypothetic catalyst.

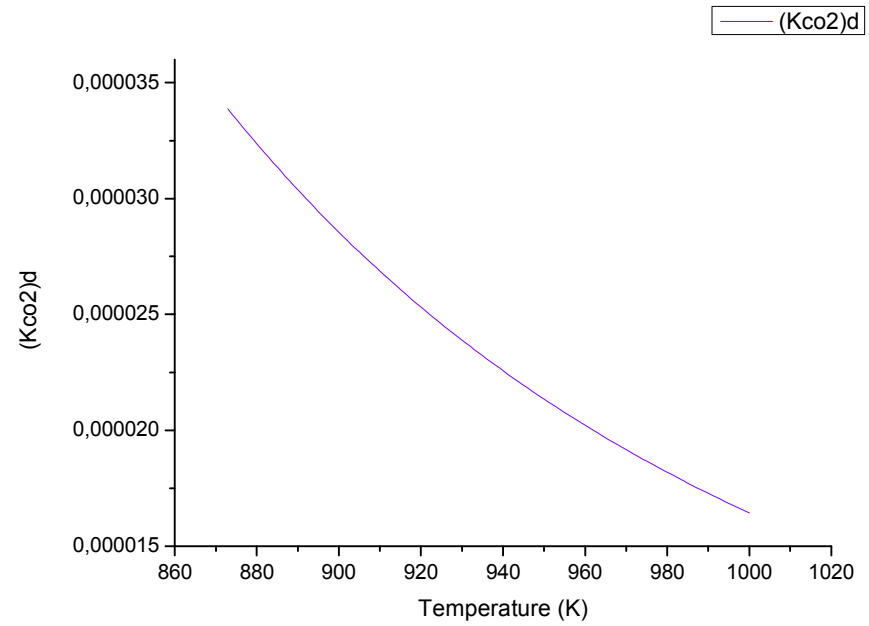


(a)

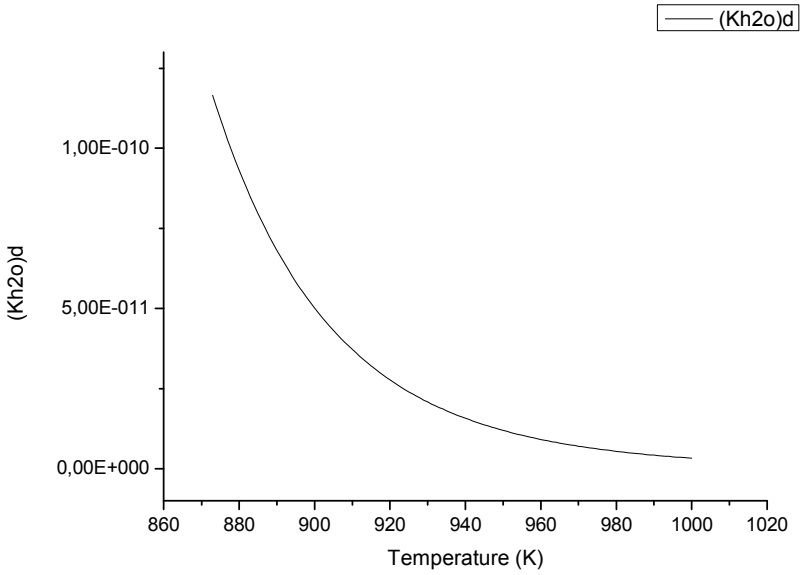


(b)

**Fig.9.** Experimental essays of RWGS reaction for FeAlNi and FeCo catalysts: (a) $CO_2$ conversion and (b) Selectivity to CO.

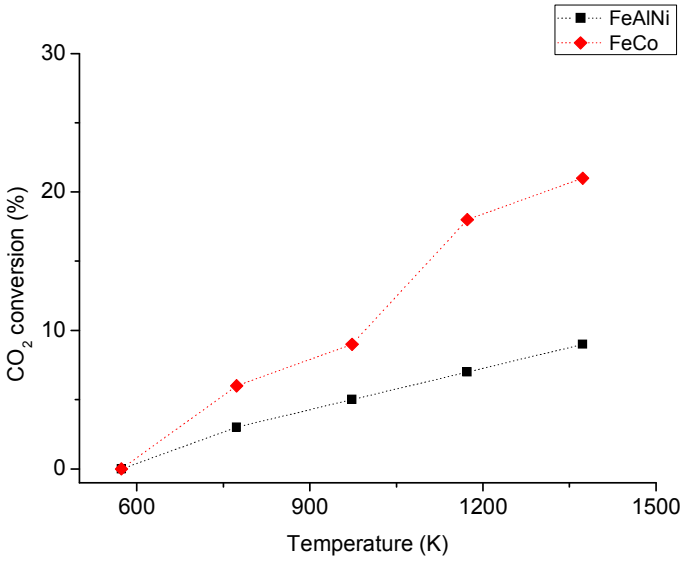


(a)

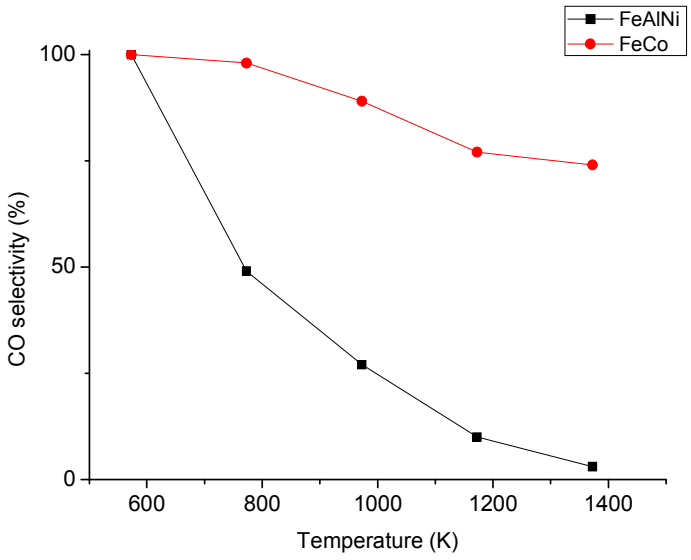

## Tables

**Table 1.** Textural parameters obtained from the nitrogen adsorption-desorption isotherms. $Sg_{BET}$ is the specific surface area calculated from BET method in the relative pressure of 0.05–0.2; Vp is the total volume calculated at relative pressure of 0.99; Dp is the pore diameter at maximum of the pore size distribution calculated by BJH method from the adsorption branch. Ethylbenzene conversion and styrene selectivity obtained with using 50 mg of fresh catalyst at 823K, $CO_2$/EB molar ratio of 30 for 5h.

| Catalyst | L[a] (nm) | $Sg_{BET}$ ($m^2.g^{-1}$) | Vp ($cm^3.g^{-1}$) | [b]Dp(Å) | [c]EB conversion (%) | [c]Styrene selectivity (%) |
|---|---|---|---|---|---|---|
| FeAlNi | 21 | 52 | 0.07 | 17 | 10 | 2 |
| FeMgZn | 44 | 46 | 0.06 | 11 | 6 | 100 |
| FeAlZn | 16 | 61 | 0.08 | 20 | 25 | 99 |
| FeAlLa | - | 70 | 0.10 | 39 | 17 | 95 |

[a] From the (311) reflection of $\gamma$-$Fe_2O_3$ observed by XRD
[b] From desorption branch of the isotherms
[c]Steady state condition

**Table 2.** Catalytic performance in the absence of $CO_2$ for the steady state condition. Reaction conditions: 50 mg of fresh catalyst, temperature of 823K over the course of 5h**.** The textural properties of the spent catalysts, after being used in the reaction in the aforesaid reaction conditions.

| Catalyst | EB conversion in the absence of $CO_2$ (%) | $Sg_{BET}$ ($m^2.g^{-1}$) | Vp ($cm^3.g^{-1}$) |
|---|---|---|---|
| FeAlNi | 20 | 19 | 0.03 |
| FeMgZn | 9 | 14 | 0.02 |
| FeAlZn | 2 | 54 | 0.07 |
| FeAlLa | - | 63 | 0.09 |

**Table 3.** Number of essays (NPt), temperature (T) and velocity constant ($k_{RGWS}$) values for RWGS reaction. The results were obtained from 400 to 1050 K with using a $CO_2/H_2$ molar ratio of 1.

| **NPt** | **T(K)** | **$k_{RGWSx}10^2$ ($s^{-1}$)** |
|---|---|---|
| 1 | 400 | 0.07 |
| 2 | 450 | 0.3 |
| 3 | 500 | 0.8 |
| 4 | 550 | 2.0 |
| 5 | 600 | 4.0 |
| 6 | 650 | 7.0 |
| 7 | 700 | 11.0 |
| 8 | 750 | 18.0 |
| 9 | 800 | 26.0 |
| 10 | 850 | 32.0 |
| 11 | 900 | 33.0 |
| 12 | 950 | 35.0 |
| 13 | 1000 | 36.0 |
| 14 | 1050 | 37.0 |

**Table 4.** Number of essays (NPt) carbon dioxide to hydrogen partial pressure ($p_{H2}/p_{CO2}$) and RWGS reaction rate.

| **NPt** | **$P_{CO2}/p_{H2}$** | **$r_{RGWSx10}^{19}$ ( kmol.$kg^{-1}$)** |
|---|---|---|
| 1 | 0.5 | 0.39 |
| 2 | 1 | 1.57 |
| 3 | 2 | 3.14 |
| 4 | 3 | 4.71 |
| 5 | 4 | 6.29 |
| 6 | 5 | 7.86 |
| 7 | 6 | 9.43 |
| 8 | 7 | 11.01 |
| 9 | 8 | 12.58 |
| 10 | 9 | 14.15 |
| 11 | 10 | 15.72 |